J. Fluid Mech. (2022), *vol*. 947, A22, doi:10.1017/jfm.2022.654

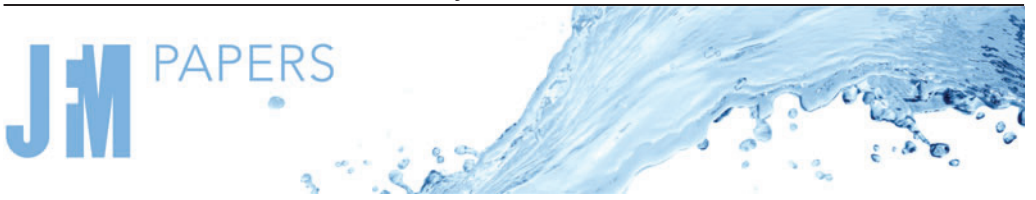

Quasi-dynamic subgrid-scale kinetic energy equation model for large-eddy simulation of compressible flows

Han Qi[1,2], **Xinliang Li**[1,2], **Running Hu**[1,2] **and Changping Yu**[1,†]

[1]LHD, Institute of Mechanics, Chinese Academy of Sciences, Beijing 100190, PR China

[2]School of Engineering Science, University of Chinese Academy of Sciences, Beijing 100049, PR China

(Received 4 January 2022; revised 25 May 2022; accepted 25 July 2022)

A quasi-dynamic subgrid-scale (SGS) kinetic energy one-equation eddy-viscosity model is introduced in this paper for large-eddy simulation (LES) of compressible flows. With the additional SGS kinetic energy equation, the SGS kinetic energy can be predicted properly. Then, using the dual constraints of SGS kinetic energy and the SGS kinetic energy flux, the eddy-viscosity model can be determined exactly. Taking a similar scheme as the expansion of the SGS stress, other unclosed quantities in the equations to be solved could be well modelled separately. Therefore, with the advance of the equations, all the model coefficients can be determined dynamically. Differing from the classic dynamic procedure, the new methodology needs no test filtering, and thus it could also be called a quasi-dynamic procedure. Using direct numerical simulation of compressible turbulent channel flow, the *a priori* test shows that the key modelled quantities of the suggested model display high correlations with the real values. In LES of compressible turbulent channel flows of the Mach number being 1.5 and 3.0, the proposed model can precisely predict some important quantities, including the mean velocity, Reynolds stress and turbulent flux, and it can also supply more abundant turbulent structures. For the compressible flat-plate boundary layer, the new model can correctly predict the transition process, mean velocity and turbulence intensities in the turbulent region. The results show that the proposed model has the advantage of scale adaptivity. Finally, the new model is applied to LES of turbulent mixing in spherical converging Richtmyer–Meshkov instability, and the accurate results show that the new model has a good ability for LES of complex fluids.

Key words: turbulence modelling

† Email address for correspondence: cpyu@imech.ac.cn

1. Introduction

Large-eddy simulation (LES) is increasingly applied to simulate high Reynolds number turbulent flows and plays an important role in science and engineering research. Although many subgrid-scale (SGS) models are applied in simulating complex flows, reliable results cannot be ensured because more current SGS models are constructed based on the assumption that the subgrid scales are approximately isotropic (Moser, Haering & Yalla 2021). In addition, most of the current SGS models were initially constructed for incompressible flows and are directly generalized to compressible flows, which means that the current models cannot exactly predict certain phenomena, such as compression shocks in compressible flows (Garnier, Adams & Sagaut 2013).

In LES, the filtered Navier–Stokes (N–S) equations contain some SGS terms for modelling. The eddy-viscosity model is the most popular SGS stress model used in practical LES because of its strong numerical robustness and simplicity (Meneveau & Katz 2000; Rozema *et al.* 2015). The Smagorinsky model (SM) (Smagorinsky 1963; Lilly 1967) is the most representative eddy-viscosity model, and it's coefficient C_{sm} can take different values empirically for different simulation cases. Metais & Lesieur (1992) obtained a new SGS eddy viscosity using a second-order structure function. Nicoud & Ducros (1999) proposed a wall-adapting local eddy-viscosity model, which can correctly predict behaviours in the near-wall region. Vreman (2004) proposed a low dissipation eddy-viscosity model (Vreman model) for turbulent shear flows, and it can also predict transitional flow well. Then, through the analysis of the singular values of the resolved velocity gradient tensor, Nicoud *et al.* (2011) proposed the σ model to improve the prediction of wall-bounded flows. According to the balance of the helicity transfer and dissipation in the inertial region and a spectral relative helicity relation, Yu *et al.* (2013) supplied a new eddy-viscosity model, which was successfully applied to simulate compressible transitional flows (Zhou *et al.* 2019). Rozema *et al.* (2015) supplied an anisotropic minimum-dissipation eddy-viscosity model, which does not need an approximation of the filter width. Recently, Leoni *et al.* (2021) introduced an eddy-viscosity model based on fractional gradients, which can provide stronger non-local correlations than traditional eddy-viscosity models. Although eddy-viscosity models are popularly adopted, they still have some drawbacks. The current eddy-viscosity models always supply pure dissipation and have low correlation with the real SGS stress, so they cannot exactly depict the characteristics of the real physical quantities in turbulence (Vreman, Geurts & Kuerten 1996; Meneveau & Katz 2000). The eddy-viscosity model cannot correctly reproduce the distributions of the SGS kinetic energy flux (KEF) and the SGS stress (Meneveau & Katz 2000). It should be noted that the KEF is a significant characteristic for SGS models in LES (Moser *et al.* 2021).

Aside from the eddy-viscosity model, there are other types of SGS model, such as the structural model and the mixed model. The scale-similarity model is one of the structural models proposed by Bardina, Ferziger & Reynolds (1984) and revised by Liu, Meneveau & Katz (1994). The gradient model (Clark, Ferziger & Reynolds 1979; Vreman *et al.* 1996) is another structural model that was derived from Taylor expansions for SGS stress using the filtered velocity. Different from the eddy-viscosity model, the scale-similarity model and gradient model have common merits in that they have a high correlation with the real SGS stress and the KEF predicted by these two structural models is also highly correlated with the real value. However, the shortcoming is that they easily lead to unstable simulation, which has been proven through linear stability analysis (Vreman *et al.* 1996). Then, several mixed models were proposed to achieve a relatively high correlation with the SGS stress and address the shortcoming of instability in simulation (Bardina *et al.* 1984;

Zang, Street & Koseff 1993; Vreman, Geurts & Kuerten 1994; Horiuti 1997). Even so, these improvement methods still have some drawbacks, such as excessive SGS dissipation (Vreman *et al.* 1996) and a deteriorated correlation (Yu, Zuoli & Xinliang 2016).

The SGS kinetic energy equation model (k-equation model) for LES was introduced by Schumann (1975) through dimensional analysis for LES of incompressible flows. Then, Yoshizawa (1985) also independently obtained the k-equation model from the two-scale direct interaction approximation. Since the k-equation model can take into account the deviation from the equilibrium state and time history effect (Horiuti & Tamaki 2013), it has been successfully applied in different types of turbulent flows (Moeng 1984; Horiuti 1985; Yoshizawa 1991; Stevens, Moeng & Sullivan 1999). The dynamic procedure was also applied to the k-equation model in incompressible turbulence (Ronchi, Ypma & Canuto 1992; Wong 1992; Ghosal *et al.* 1995; Kim & Menon 1999). Pomraning & Rutland (2002) applied infinite series expansions to model unclosed quantities and suggested a new dynamic one-equation non-viscosity LES model. At the same time, the k-equation model was generalized to compressible flows with compressible effects considered in all SGS terms (Patel, Stone & Menon 2003), and the compressible k-equation model was also successfully applied to simulate supersonic combustion flows (Genin & Menon 2010). Although the k-equation model has been successfully applied to different kinds of flows, the modelling for the unclosed terms in the SGS kinetic energy equation is not satisfactory. For most studies, the unclosed terms in the equation are grouped into production and dissipation terms. Unlike in previous research, Chai & Mahesh (2012) proposed a new dynamic k-equation model (dk-equation model) for LES of compressible turbulence, where each of the unclosed quantities is modelled independently to improve the effects of predictions.

To effectively improve the simulation, the dynamic procedure is often used to determine the coefficients in SGS models. Based on the assumption of scale invariance, the dynamic procedure can determine the coefficient of the SGS model with the aid of the Germano identity (Germano *et al.* 1991; Germano 1992). Later, Lilly (1992), Ghosal *et al.* (1995) and Meneveau, Lund & Cabot (1996) modified the method, and the coefficient could be obtained locally. Porte-Agel, Meneveau & Parlange (2000) supplied a scale-dependent dynamic SGS model in which the model coefficient varies with scale. Considering the ratio of the SGS energy dissipation across an arbitrary grid scale to the resolved viscous dissipation, Yu, Xiao & Li (2017) proposed a scale-adaptive dynamic SGS model, which has been proven to be better than traditional dynamic SGS models. The dynamic procedure can also be applied to model the SGS heat flux. Moin *et al.* (1991) proposed a dynamic linear eddy thermal diffusivity model. Then, Wang *et al.* (2008) supplied three new dynamic tensor thermal diffusivity SGS heat flux models based on the general gradient diffusion hypothesis. Subsequently, Meneveau (2012) restated the Germano identity in a generalized form that can be applied to the dynamic procedure for any scalar flux model.

As discussed above, both the eddy-viscosity model and the gradient model have distinctive merits and defects. This study proposes a new quasi-dynamic SGS kinetic energy equation model (QKM) combining the advantages of both the eddy-viscosity model and the gradient model based on the SGS kinetic energy equation. The newly proposed model is tested in three different representative compressible flows.

The structure of this paper is as follows: the governing equations and SGS models are introduced in § 2. The derivation of the QKM is supplied in § 3. In § 4, we test the new model compared with the traditional dynamic models and give detailed analyses. Finally, the conclusions are provided in § 5.

2. Governing equations and SGS models

The filtered N–S equations for compressible flows in LES take the form

$$\frac{\partial \bar{\rho}}{\partial t} + \frac{\partial \bar{\rho}\tilde{u}_i}{\partial x_j} = 0, \tag{2.1}$$

$$\frac{\partial \bar{\rho}\tilde{u}_i}{\partial t} + \frac{\partial \bar{\rho}\tilde{u}_i\tilde{u}_j}{\partial x_j} = -\frac{\partial \bar{p}}{\partial x_i} + \frac{\partial \tilde{\sigma}_{ij}}{\partial x_j} - \frac{\partial \tau_{ij}}{\partial x_j}, \tag{2.2}$$

$$\frac{\partial \bar{\rho}\tilde{E}}{\partial t} + \frac{\partial (\bar{\rho}\tilde{E} + \bar{p})\tilde{u}_j}{\partial x_j} = -\frac{\partial \tilde{q}_j}{\partial x_j} + \frac{\partial \tilde{\sigma}_{ij}\tilde{u}_i}{\partial x_j} - \frac{\partial C_p Q_j}{\partial x_j} - \frac{\partial J_j}{\partial x_j}, \tag{2.3}$$

where $\bar{(\cdot)}$ represents spatial filtering with a low-pass filter at scale Δ and $\tilde{(\cdot)}$ represents density-weighted (Favre) filtering ($\tilde{\phi} = \overline{\rho\phi}/\bar{\rho}$). In the filtered N–S equations, $\bar{\rho}$, $\tilde{u}_i$, $\bar{p}$ and $\tilde{E}$ are the filtered density, velocity, pressure and total energy, respectively. In this study, (2.3) is obtained by applying the filtering operator to the total energy equation, and the form of the filtered total energy can be represented as $\bar{\rho}\tilde{E} = \bar{\rho}C_v\tilde{T} + \frac{1}{2}\bar{\rho}\tilde{u}_i\tilde{u}_i + \bar{\rho}k_{sgs}$ (Martín, Piomelli & Candler 2000; Garnier *et al.* 2013), where k_{sgs} is the SGS kinetic energy and can be expressed as

$$\bar{\rho}k_{sgs} = \tfrac{1}{2}\bar{\rho}(\widetilde{u_i u_i} - \tilde{u}_i\tilde{u}_i). \tag{2.4}$$

The filtered pressure is determined by $\bar{p} = \bar{\rho}R\tilde{T}$, where R is the specific gas constant and $\tilde{T}$ is the filtered temperature. The resolved viscous stress $\tilde{\sigma}_{ij}$ and heat flux $\tilde{q}_j$ are expressed as

$$\tilde{\sigma}_{ij} = 2\mu(\tilde{T})\widetilde{\mathbb{S}}_{ij}, \tag{2.5}$$

$$\widetilde{\mathbb{S}}_{ij} = \tilde{S}_{ij} - \frac{1}{3}\delta_{ij}\tilde{S}_{kk} = \frac{1}{2}\left(\frac{\partial \tilde{u}_i}{\partial x_j} + \frac{\partial \tilde{u}_j}{\partial x_i}\right) - \frac{1}{3}\frac{\partial \tilde{u}_k}{\partial x_k}\delta_{ij}, \tag{2.6}$$

$$\tilde{q}_j = \frac{C_p\mu(\tilde{T})}{P_r}\frac{\partial \tilde{T}}{\partial x_j}, \tag{2.7}$$

where the molecular viscosity μ takes the form $\mu = (1/Re)(\tilde{T}/\tilde{T}_\infty)^{3/2}((\tilde{T}_\infty + T_s)/(\tilde{T} + T_s))$ according to Sutherland's law, in which T_s is 110.3 K, the Reynolds number Re takes the form $Re = \rho_\infty U_\infty L/\mu_\infty$ and $\tilde{S}_{ij} = \frac{1}{2}(\partial\tilde{u}_i/\partial x_j + \partial\tilde{u}_j/\partial x_i)$ is the resolved strain-rate tensor. Here, C_p is the specific heat at constant pressure and P_r is the molecular Prandtl number. In (2.2) and (2.3), there are still some SGS unclosed terms, which are the SGS stress

$$\tau_{ij} = \bar{\rho}(\widetilde{u_i u_j} - \tilde{u}_i\tilde{u}_j), \tag{2.8}$$

the SGS heat flux

$$Q_j = \bar{\rho}(\widetilde{u_j T} - \tilde{u}_j\tilde{T}), \tag{2.9}$$

and the SGS turbulent diffusion term

$$J_j = \tfrac{1}{2}\bar{\rho}(\widetilde{u_i u_i u_j} - \widetilde{u_i u_i}\tilde{u}_j). \tag{2.10}$$

All the unclosed terms need to be modelled using the filtered quantities. Next, we will discuss the modelling of these terms in detail.

Because of its numerical robustness and simplicity, the eddy-viscosity model is most often adopted in practical simulations (Meneveau & Katz 2000; Rozema *et al.* 2015).

The eddy-viscosity model is a phenomenological model, and the proposal of this model is based on a Boussinesq-type hypothesis, which is

$$\tau_{ij}^{mod} - \tfrac{1}{3}\delta_{ij}\tau_{kk}^{mod} = -2\mu_{sgs}\widetilde{\mathbb{S}}_{ij}, \tag{2.11}$$

where τ_{kk}^{mod} is the isotropic part of the SGS stress model.

Comparing (2.8) and (2.4), we find that the isotropic part of SGS stress τ_{kk} and the SGS kinetic energy k_{sgs} have the relationship as

$$\tau_{kk} = 2\bar{\rho}k_{sgs}. \tag{2.12}$$

In the eddy-viscosity model, the SM is the typical model and widely exists in LES of different types of flows (Smagorinsky 1963). Therefore, the SM is chosen as the object model in this study. In the SM, the eddy viscosity can be written as

$$\mu_{sgs}^{mod} = \bar{\rho}C_{sm}\Delta^2|\tilde{S}|, \tag{2.13}$$

where

$$|\tilde{S}| = \sqrt{2\tilde{S}_{ij}\tilde{S}_{ij}}, \tag{2.14}$$

and C_{sm} is the coefficient of the anisotropic part of the SM. The isotropic part of the SGS tensor for the SM is

$$\tau_{kk}^{mod} = 2C_I\bar{\rho}\Delta^2|\tilde{S}|^2, \tag{2.15}$$

where C_I is the coefficient of the isotropic part of the SM (Yoshizawa 1986).

For the SGS heat flux model, we still take the commonly used SGS diffusion model (Moin *et al.* 1991) as

$$Q_j^{mod} = -\frac{\mu_{sgs}}{Pr_{sgs}}\frac{\partial\tilde{T}}{\partial x_j}, \tag{2.16}$$

where Pr_{sgs} is the SGS Prandtl number.

3. Derivation of the QKM

3.1. *The SGS kinetic energy equation*

Since the k-equation model was proposed by Schumann (1975) and Yoshizawa (1985), it has been successfully used in LES of incompressible and compressible flows (Pomraning & Rutland 2002; Genin & Menon 2010; Chai & Mahesh 2012). Consequently, we will attach the SGS kinetic energy equation to the N–S equations to improve the precision of the SGS models in this study.

The derivation of the compressible SGS kinetic energy equation has been reported by Chai & Mahesh (2012), and the equation can be written as

$$\frac{\partial\bar{\rho}k_{sgs}}{\partial t} + \frac{\partial\bar{\rho}k_{sgs}\widetilde{u}_j}{\partial x_j} = -\Pi_\Delta - \frac{\partial J_j}{\partial x_j} - \varepsilon_s - \varepsilon_d + \Pi_p + \frac{\partial\zeta_j}{\partial x_j} + \frac{\partial}{\partial x_j}\left[\mu(\tilde{T})\frac{\partial k_{sgs}}{\partial x_j}\right], \tag{3.1}$$

where

$$\Pi_\Delta = \tau_{ij}\frac{\partial \widetilde{u_i}}{\partial x_j}, \tag{3.2}$$

$$\varepsilon_s = 2\mu(\tilde{T})(\widetilde{\mathbb{S}_{ij}\mathbb{D}_{ij}} - \widetilde{\mathbb{S}}_{ij}\widetilde{\mathbb{D}}_{ij}), \tag{3.3}$$

$$\mathbb{D}_{ij} = \frac{\partial u_i}{\partial x_j} - \frac{1}{3}\delta_{ij}\frac{\partial u_k}{\partial x_k}, \tag{3.4}$$

$$\varepsilon_d = \frac{\partial}{\partial x_j}\left[\frac{5}{3}\mu(\tilde{T})(\widetilde{u_j\frac{\partial u_k}{\partial x_k}} - \tilde{u}_j\frac{\partial \tilde{u}_k}{\partial x_k})\right], \tag{3.5}$$

$$\Pi_p = \overline{p\frac{\partial u_k}{\partial x_k}} - \bar{p}\frac{\partial \tilde{u}_k}{\partial x_k}, \tag{3.6}$$

and

$$\zeta_j = \tau_{ij}\tilde{u}_i + \mu(\tilde{T})\frac{\partial}{\partial x_i}\left(\frac{\tau_{ij}}{\bar{\rho}}\right) + RQ_j. \tag{3.7}$$

In (3.1) to (3.7), there are some other unclosed quantities, which are the KEF Π_Δ across the mesh scale Δ, the solenoidal dissipation ε_s, the dilatational dissipation ε_d and the pressure dilatation Π_p (Chai & Mahesh 2012). Equation (3.1) is the exact form of the SGS kinetic energy equation. To precisely predict the key quantities in compressible turbulence, we will construct each unclosed quantity individually.

3.2. *The quasi-dynamic procedure and modelling*

Since the turbulent cascade description was proposed by Richardson, the turbulent cascade has become the most fundamental conception of turbulent theory. The KEF is the core physical quantity for the turbulent cascade and is also a critical characteristic for SGS modelling in LES (Moser *et al.* 2021). In past studies, several modelling methods for KEF have been developed, such as parametrization based on the tensor eddy viscosity (Borue & Orszag 1998), a multi-scale gradient expansion (Eyink 2006) and artificial neural networks (Yuan, Xie & Wang 2020).

As presented in (3.2), SGS stress τ_{ij} is the only unclosed quantity in the KEF. To obtain the resolved form of τ_{ij}, the infinite series expansion (Bedford & Yeo 1993) is applied to expand it. The infinite series expansion is expressed as

$$\overline{fg} - \bar{f}\bar{g} = \alpha\frac{\partial \bar{f}}{\partial x_k}\frac{\partial \bar{g}}{\partial x_k} + \frac{1}{2!}(\alpha)^2\frac{\partial^2 \bar{f}}{\partial x_k \partial x_l}\frac{\partial^2 \bar{g}}{\partial x_k \partial x_l} + \frac{1}{3!}(\alpha)^3\frac{\partial^3 \bar{f}}{\partial x_k \partial x_l \partial x_m}\frac{\partial^3 \bar{g}}{\partial x_k \partial x_l \partial x_m} + \cdots, \tag{3.8}$$

where

$$\alpha(y) = \int_{-\infty}^{\infty} 2x^2 G(x, y)\,\mathrm{d}x. \tag{3.9}$$

Here, $G(x, y)$ is the kernel of the filter, and f and g can be vectors or scalars. In this study, $G(x, y)$ is designated as the box filter for the case of *a priori* test and the grid filter (Tejada-Martínez & Jansen 2004) is used in the LES cases.

The parameter α can be taken as

$$\alpha = C_0\Delta_k^2, \tag{3.10}$$

where Δ_k is the grid width in the x_k direction.

Through the method of (3.8), τ_{ij} can be expanded as

$$\tau_{ij} = C_0\Delta_k^2\bar{\rho}\frac{\partial\tilde{u}_i}{\partial x_k}\frac{\partial\tilde{u}_j}{\partial x_k} + \frac{1}{2!}(C_0^2\Delta_k^2\Delta_l^2)\bar{\rho}\frac{\partial^2\tilde{u}_i}{\partial x_k\partial x_l}\frac{\partial^2\tilde{u}_j}{\partial x_k\partial x_l} + \cdots. \tag{3.11}$$

Since the other higher-order terms are small enough compared with the first term of (3.11) (Vreman *et al.* 1996), and also for avoiding the complexity of additional boundary conditions, we only reserve the first term in (3.11) as the approximation of τ_{ij}

$$\tau_{ij} \approx C_0\Delta_k^2\bar{\rho}\frac{\partial\tilde{u}_i}{\partial x_k}\frac{\partial\tilde{u}_j}{\partial x_k}. \tag{3.12}$$

When $C_0 = 1/12$, (3.12) can take the same form as the gradient model ($\tau_{ij}^{mod} = \frac{1}{12}\Delta_k^2\bar{\rho}(\partial_k\tilde{u}_i)(\partial_k\tilde{u}_j)$) (Clark *et al.* 1979; Vreman *et al.* 1996).

Then the approximation of KEF Π_Δ is

$$\Pi_\Delta = C_0\Delta_k^2\bar{\rho}\frac{\partial\tilde{u}_i}{\partial x_k}\frac{\partial\tilde{u}_j}{\partial x_k}\tilde{S}_{ij}. \tag{3.13}$$

From (3.12), we find that

$$\tau_{kk} = C_0\Delta_l^2\bar{\rho}\frac{\partial\tilde{u}_k}{\partial x_l}\frac{\partial\tilde{u}_k}{\partial x_l}. \tag{3.14}$$

Comparing (2.12) with (3.14), we can confirm the real value of C_0 in LES as

$$C_0 = \frac{2k_{sgs}}{\Delta_l^2\dfrac{\partial\tilde{u}_k}{\partial x_l}\dfrac{\partial\tilde{u}_k}{\partial x_l}}, \tag{3.15}$$

which is the constraint condition for obtaining more precise τ_{ij}, Π_Δ and other unclosed quantities.

As discussed in the introduction, the gradient model has a high correlation with the real SGS stress but is unstable in practical simulations (Vreman *et al.* 1996). Thus, we can deduce that the approximated τ_{ij} in (3.12) has the same advantages and disadvantages as the gradient model. The SM has low correlation with the real SGS stress but strong numerical robustness in simulations (Meneveau & Katz 2000; Moser *et al.* 2021). To obtain a more accurate KEF across the scale Δ (Π_Δ) from the SM in LES, we use (3.13) to constrain the SM as

$$\Pi_\Delta = \Pi_\Delta^{SM}, \tag{3.16}$$

where

$$\Pi_\Delta^{SM} = \Pi_\Delta^{SMA} + \Pi_\Delta^{SMI}, \tag{3.17}$$

$$\Pi_\Delta^{SMA} = -2C_{sm}\bar{\rho}\Delta^2|\tilde{S}|\widetilde{\mathbb{S}}_{ij}\tilde{S}_{ij}, \quad \text{and} \quad \Pi_\Delta^{SMI} = \tfrac{2}{3}C_I\bar{\rho}\Delta^2|\tilde{S}|^2\delta_{ij}\tilde{S}_{ij}. \tag{3.18a,b}$$

In (3.17)–(3.18*a*,*b*), Π_Δ^{SMA} and Π_Δ^{SMI} are the anisotropic part and the isotropic part of Π_Δ^{SM}, respectively. Π_Δ also has an anisotropic part Π_Δ^{A} and isotropic part Π_Δ^{I} as

$$\Pi_\Delta^{A} = \left(C_0\Delta_k^2\bar{\rho}\frac{\partial\tilde{u}_i}{\partial x_k}\frac{\partial\tilde{u}_j}{\partial x_k} - \frac{2}{3}\delta_{ij}\bar{\rho}k_{sgs}\right)\tilde{S}_{ij}, \tag{3.19}$$

$$\Pi_\Delta^{I} = \tfrac{2}{3}\delta_{ij}\bar{\rho}k_{sgs}\tilde{S}_{ij}. \tag{3.20}$$

To accomplish the second constraint, we let $\Pi_{\Delta}^{A} = \Pi_{\Delta}^{SMA}$ and the model coefficient C_{sm} of the SM can be rewritten as

$$C_{sm} = -\frac{\left(C_0\Delta_k^2\bar{\rho}\dfrac{\partial\tilde{u}_i}{\partial x_k}\dfrac{\partial\tilde{u}_j}{\partial x_k} - \dfrac{2}{3}\delta_{ij}\bar{\rho}k_{sgs}\right)\tilde{S}_{ij}}{2\bar{\rho}\Delta^2|\tilde{S}|\widetilde{\mathbb{S}}_{ij}\widetilde{S}_{ij}}. \tag{3.21}$$

The isotropic part of SM is obtained directly from (2.12) instead of (2.15) in this paper.

For the other unclosed terms, their resolved forms could also be obtained from the same infinite expansion of (3.8) (Pomraning & Rutland 2002). We know that the α of the different expanded quantities should be the same when using the same filter on a designated grid point in theory. Therefore, in practical simulations, we could assume that C_0 is the same for the different expanded quantities. In this study, we introduce the SGS kinetic energy to obtain C_0 of SGS stress. Therefore, the C_0 of SGS stress could be suitable for other SGS terms under the assumption.

To model the SGS heat flux, we can apply the expansion method of (3.8) to expand the SGS heat flux as

$$Q_j = C_0\Delta_k^2\bar{\rho}\frac{\partial\tilde{u}_j}{\partial x_k}\frac{\partial\tilde{T}}{\partial x_k}. \tag{3.22}$$

Adopt a similar quasi-dynamic procedure for the SGS stress model (set $\partial Q_j^{mod}/\partial x_j = \partial Q_j/\partial x_j$), and the SGS Prandtl number in (2.16) can be determined as

$$Pr_{sgs} = -\frac{\partial\left(\nu_{sgs}\dfrac{\partial\tilde{T}}{\partial x_j}\right)/\partial x_j}{\partial\left(C_0\Delta_k^2\dfrac{\partial\tilde{u}_j}{\partial x_k}\dfrac{\partial\tilde{T}}{\partial x_k}\right)/\partial x_j}, \tag{3.23}$$

where $\nu_{sgs} = \mu_{sgs}/\bar{\rho}$.

For the SGS turbulent diffusion term in (2.10), we can use the same strategy as $J_j = \tau_{ij}\tilde{u}_i$ (Martín *et al.* 2000). Therefore, we have modelled all the unclosed quantities in the filtered N–S equations.

For the unclosed quantities Π_p, ε_s and ε_d in the SGS kinetic energy equation (3.1), we still apply the same expansion method as (3.8) to model them.

The pressure diffusion Π_p can be modelled as

$$\Pi_p \approx C_0\Delta_m^2\frac{\partial\bar{p}}{\partial x_m}\frac{\partial^2\tilde{u}_k}{\partial x_m\partial x_k}. \tag{3.24}$$

The solenoidal dissipation ε_s can be modelled as

$$\varepsilon_s \approx 2C_0\Delta_k^2\mu(\tilde{T})\frac{\partial\widetilde{\mathbb{S}}_{ij}}{\partial x_k}\frac{\partial\widetilde{\mathbb{D}}_{ij}}{\partial x_k}. \tag{3.25}$$

The dilatational dissipation ε_d can be modelled as

$$\varepsilon_d \approx \frac{5}{3}\frac{\partial}{\partial x_j}\left[C_0\Delta_l^2\mu(\tilde{T})\frac{\partial\tilde{u}_j}{\partial x_l}\frac{\partial^2\tilde{u}_k}{\partial x_k\partial x_l}\right]. \tag{3.26}$$

Thus far, we have obtained all the unclosed quantities in the filtered N–S equations and the SGS kinetic energy equation, and the QKM has been completely modelled. Next, we will test and analyse the proposed model for different cases of compressible flows.

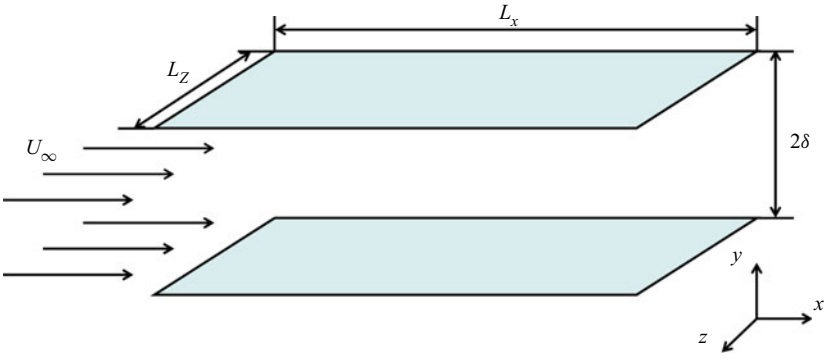

Figure 1. Schematic diagram for the compressible turbulent channel flow.

4. Application tests and analyses

In this section, the new model will first be tested in fully developed compressible turbulent channel flows at the Mach number being 1.5 and 3. Then it will be applied in LES of the flow of the compressible flat-plate boundary layer. Finally, to see the performance of the proposed model in a more complicated case, the new model will be tested in the flow of spherical converging Richtmyer–Meshkov instability.

4.1. *Application in compressible turbulent channel flow*

In this part, a fully developed compressible turbulent channel flow (Coleman *et al.* 1995; Morinishi, Tamano & Nakabayashi 2004) is selected as the first test case for QKM. Regarding the compressible turbulent channel flow, the size of the computational domain is $L_x \times L_y \times L_z = 4\pi \times 2 \times 4\pi/3$, the Mach number is $Ma = 1.5$, the bulk Reynolds number Re is 3000, the friction Reynolds number $Re_\tau = u_\tau \delta/\nu$ is 220 ($u_\tau = \sqrt{\tau_w/\rho_w}$ is the friction velocity, τ_w is the wall shear stress, ρ_w is the wall density, δ is the channel half-width and ν is the kinematic viscosity; $Re_\tau = 220$ is the result of the simulations), the friction Mach number $Ma_\tau = u_\tau/a_w$ is approximately 0.0815 (a_w is the sound speed based on the wall temperature), the Prandtl number $Pr = \mu C_p \kappa$ is 0.7 (κ is the thermal conductivity and C_p is the specific heat at constant pressure) and the ratio of specific heats is $\gamma = C_p/C_v = 1.4$ (C_v is the specific heat at constant volume). The flow is driven by a uniform body force. Periodic boundary conditions are applied in the streamwise and spanwise directions. The no-slip boundary condition and isothermal-wall boundary conditions are utilized on the walls. For LES, the filtered N–S equations are solved using a high-precision non-dimensional finite difference solver in Cartesian coordinates. In this solver, a sixth-order central difference scheme is applied to discretize both the convective and viscous terms, and the third-order Runge–Kutta scheme is used for the time advance. The dynamic Smagorinsky model (DSM) and the dk-equation model (Chai & Mahesh 2012) are compared with the new model. A box filter is used for test filtering for the Germano identity of the dynamic procedure, where the test-filter width is 2Δ ($\Delta = (\Delta_x \Delta_y \Delta_z)^{1/3}$). Tables 1 to 4 show the grid settings and main parameters for direct numerical simulation (DNS) and LES in this case, respectively (u_c, ρ_c and T_c are the streamwise velocity, density and temperature at the midplane of the channel flow). Figure 1 shows a schematic diagram of the compressible turbulent channel flow.

First, using an *a priori* test, we will discuss the correlation of the different unclosed quantities modelled by DSM, dk-equation model and QKM with the real values and a box

	Grids	Δx^+	Δy^+_{min}	Δy^+_{max}	Δz^+
DNS	$900 \times 201 \times 300$	2.99	0.32	4.54	2.99
LES-grid1	$64 \times 87 \times 64$	42.2	0.76	10.3	14.08
LES-grid2	$48 \times 65 \times 48$	57.5	1.07	18.1	19.18
LES-grid3	$48 \times 49 \times 48$	57.5	1.41	18.8	19.18

Table 1. The grid settings and grid resolutions of the simulations in the compressible turbulent channel flow ($Ma = 1.5$, $Re = 3000$).

	Re_τ	Ma_τ	$-B_q$	u_c/U_m	ρ_c/ρ_w	T_c/T_w
DNS	220	0.0815	0.0445	1.156	0.717	1.388
DSM	213	0.0810	0.0434	1.157	0.719	1.382
dk-equation model	215	0.0812	0.0441	1.155	0.718	1.388
QKM	220	0.0817	0.0446	1.155	0.718	1.388

Table 2. The main parameters for the simulations in the compressible turbulent channel flow for DNS and LES-grid1 ($Ma = 1.5$, $Re = 3000$).

	Re_τ	Ma_τ	$-B_q$	u_c/U_m	ρ_c/ρ_w	T_c/T_w
DSM	208	0.0804	0.0429	1.158	0.719	1.373
dk-equation model	210	0.0805	0.0431	1.155	0.718	1.385
QKM	221	0.0817	0.0447	1.155	0.718	1.387

Table 3. The main parameters for the simulations in the compressible turbulent channel flow for LES-grid2 ($Ma = 1.5$, $Re = 3000$).

	Re_τ	Ma_τ	$-B_q$	u_c/U_m	ρ_c/ρ_w	T_c/T_w
DSM	201	0.0791	0.0417	1.159	0.726	1.382
dk-equation model	208	0.0775	0.0423	1.152	0.719	1.383
QKM	218	0.0818	0.0427	1.155	0.718	1.385

Table 4. The main parameters for the simulations in the compressible turbulent channel flow for LES-grid3 ($Ma = 1.5$, $Re = 3000$).

filter is adopted in the streamwise and spanwise directions. The correlation coefficient is defined as

$$\beta = \frac{\langle (M - \langle M \rangle)(R - \langle R \rangle) \rangle}{[\langle (M - \langle M \rangle)^2 \rangle \langle (R - \langle R \rangle)^2 \rangle]^{1/2}}, \tag{4.1}$$

where $\langle \cdot \rangle$ denotes the time averaging plus space averaging in the streamwise and the spanwise directions in *a priori* tests on every plane of the turbulent channel flow.

Figure 2(*a–d*) shows the correlation coefficients of the KEF, the wall-normal SGS heat flux, the components of SGS stress τ_{12} and τ_{22} obtained from the DSM, dk-equation model and QKM using the *a priori* test at the scale of $6\Delta_z$. In figure 2(*a*,*b*), we can see that all the modelled quantities from QKM have very high correlations with the real values and all the correlation coefficients are almost higher than 0.95 along the wall-normal direction. On the contrary, the correlation coefficients of these quantities from the DSM

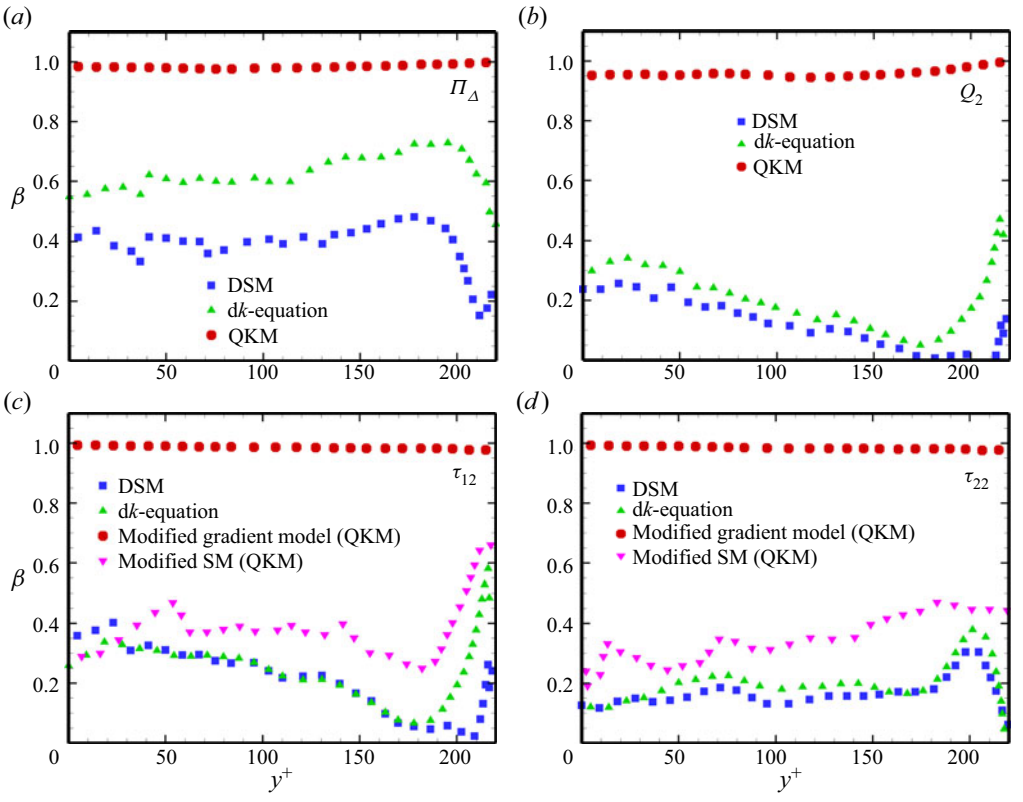

Figure 2. Correlation coefficients of different quantities from the DSM, dk-equation model and QKM obtained *a priori*: (*a*) the KEF Π_Δ; (*b*) the wall-normal SGS heat flux Q_2; (*c*) the component of SGS stress τ_{12}; (*d*) the component of SGS stress τ_{22}.

and dk-equation model are much lower. Figure 2(*c*,*d*) shows that the modified gradient model from QKM still has high correlations with the real SGS stress and the modified SM has better correlations with the real values than the DSM and dk-equation model do. We also give the correlation coefficients of the unclosed quantities in the SGS kinetic energy equation in figure 3. The correlation coefficient of the SGS turbulent diffusion term $\partial J_j/\partial x_j$ in figure 3(*d*) is nearly 1.0. The correlation coefficients of the other quantities (the pressure diffusion Π_p, the solenoidal dissipation ε_s and the dilatational dissipation ε_d) are also relatively high. From all the results of the *a priori* test, we can estimate that the QKM has high similarity with the unclosed quantities in the equations.

The real value of the coefficient C_0 obtained from (3.15) and the C_0 of the different expanded terms τ_{ij}, Q_j, Π_p, ε_s and ε_d using the *a priori* test are displayed in figure 4. From the figure, we can see that all the profiles of C_0 from the expanded terms have good agreement with the profile of the real C_0, including the trend and value. Therefore, the *a priori* results further verify the validity of our assumption. Next, we will discuss the results of the *a posterior* test in the channel flow of $Ma = 1.5$.

The profiles of the van Driest transformed mean velocity ($U_{vd} = \int_0^U \sqrt{\langle\rho\rangle/\rho_w}\,\mathrm{d}\langle U\rangle$) and the mean temperature $T_{av}^+ = (T_w - \langle T\rangle)/T_\tau$ obtained from DNS, the QKM, the dk-equation model and the DSM are compared for three LES grid resolutions in figure 5. Here, $T_\tau = B_q T_w$ is the friction temperature, $B_q = q_w/(\rho_w c_p u_\tau T_w)$ is the non-dimensional heat flux and q_w is the wall-normal heat flux. For LES-grid1, shown in figure 5(*a*1,*a*2),

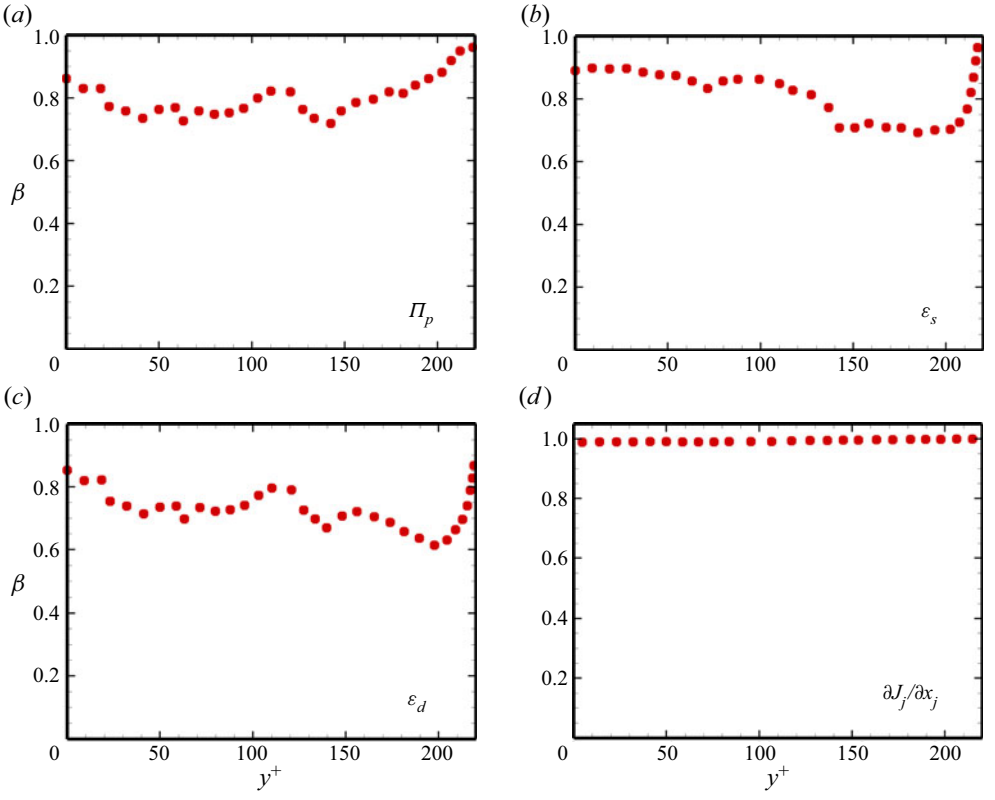

Figure 3. Correlation coefficients of the different terms in the SGS kinetic equation from the QKM obtained *a priori*: (*a*) the pressure diffusion term Π_p; (*b*) the solenoidal dissipation term ε_s; (*c*) the dilatational dissipation term ε_d; (*d*) the SGS turbulent diffusion term $\partial J_j/\partial x_j$.

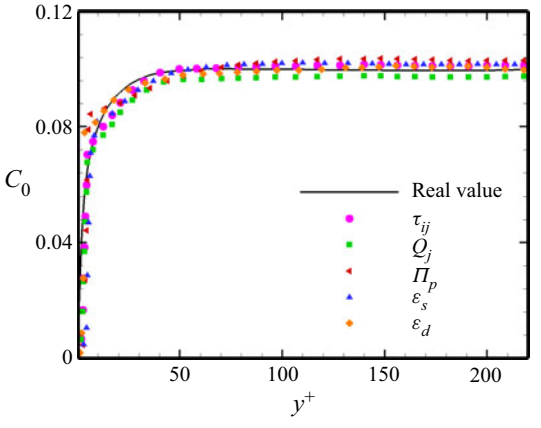

Figure 4. The coefficient C_0 of the different expanded terms and the real value obtained *a priori* using the DNS data.

we can see that all the SGS models can well predict the mean velocity and temperature, and the QKM behaves a little better than the other SGS models. From figure 5(*b*1,*b*2), we can see that the results from all the models on LES-grid2 and the DNS results present little difference in the viscous sub-layer and the buffer regions. However, in the log-law region, the QKM predicts the velocity profile perfectly and clearly performs better than the other

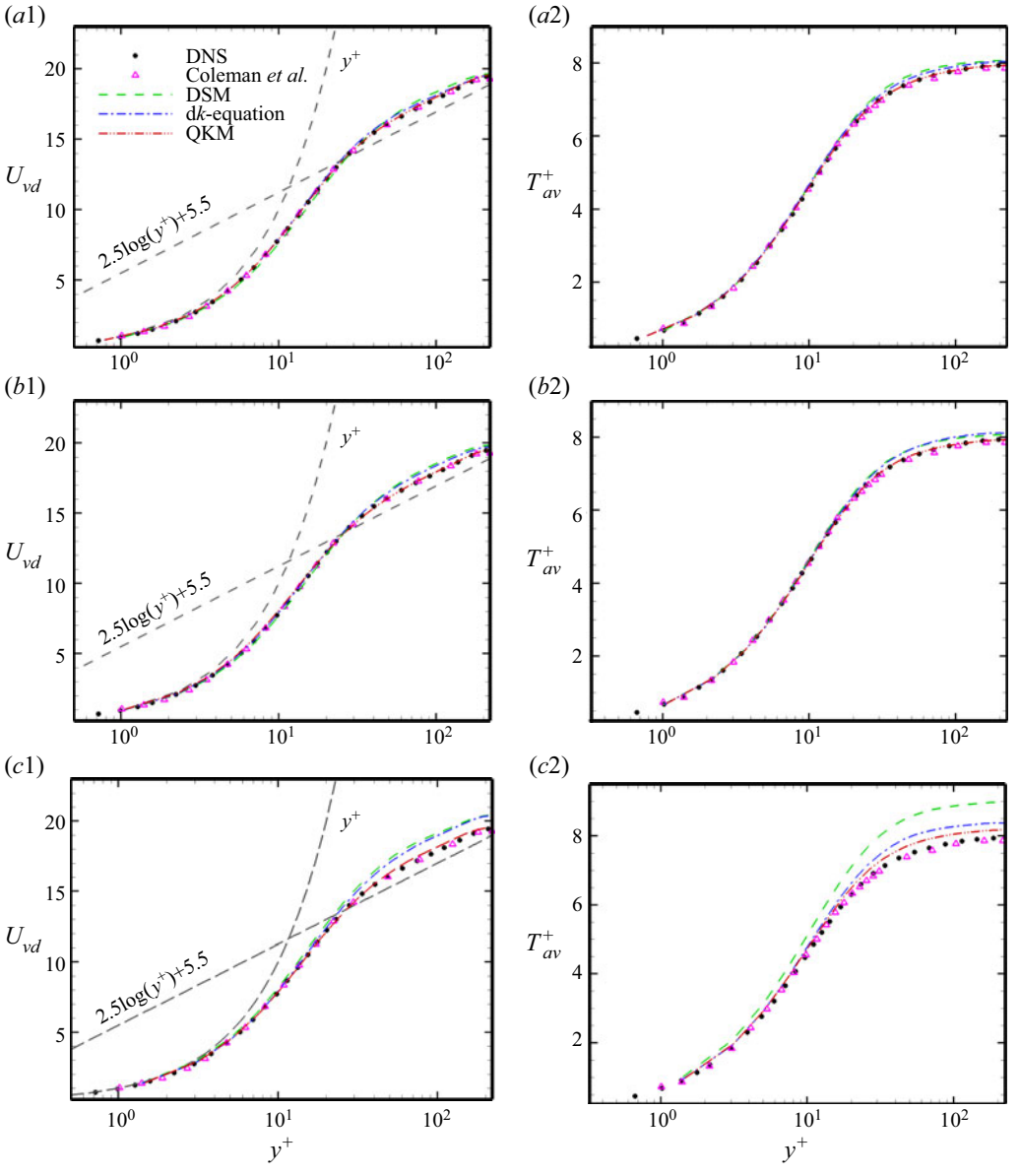

Figure 5. The van Driest transformed mean velocity U_{vd} profiles and the profiles of the mean temperature T^+_{av}, which are predicted from the DSM, dk-equation model and QKM, are compared with those of DNS: (a1) and (a2) show the case of LES-grid1; (b1) and (b2) show the case of LES-grid2; (c1) and (c2) show the case of LES-grid3. The velocity and temperature profiles from Coleman, Kim & Moser (1995) are also given here.

two models. In figure 5(c1,c2), we can see that the results from QKM are still close to the DNS results and are obviously better than those of the other two models. In short, as the grid scale decreases, the QKM can maintain good predictive ability, which is significantly better than those of the other two models, and the dk-equation model is better than the DSM. These results show that the QKM has a certain characteristic of scale adaptivity.

Next, we will perform analyses according to the results of LES-grid2 for the case of $Ma = 1.5$.

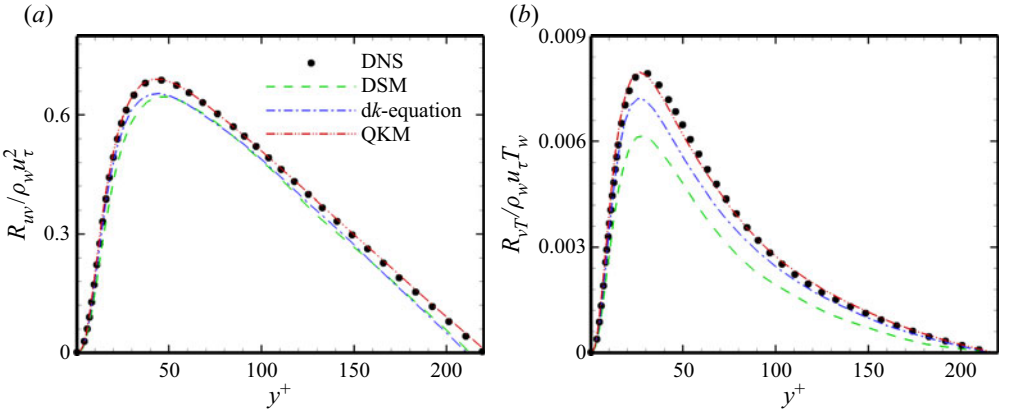

Figure 6. The profiles of the total Reynolds stress normalized by ρ_w and u_τ, and the total turbulent heat flux normalized by ρ_w, u_τ and T_w from DNS and different SGS models in the case of LES-grid2.

In compressible turbulence, if the property of ergodicity is assumed, the total Reynolds stress could be expressed as

$$R_{ij} = \langle\bar{\rho}\rangle(\{\widetilde{u_i u_j}\} - \{\widetilde{u}_i\}\{\widetilde{u}_j\}) = R_{ij}^{LES} + \langle\tau_{ij}\rangle, \tag{4.2}$$

where

$$R_{ij}^{LES} = \langle\bar{\rho}\rangle(\{\widetilde{u}_i\widetilde{u}_j\} - \{\widetilde{u}_i\}\{\widetilde{u}_j\}) \tag{4.3}$$

is the resolved Reynolds stress, and $\{\cdot\}$ denotes the Favre averaging ($\{\phi\} = \langle\rho\phi\rangle/\langle\rho\rangle$). Figure 6($a$) displays the normalized total Reynolds stress $R_{uv}/(\rho_w u_\tau^2)$ from DNS and the different models. In figure 6(a), the QKM shows better agreements than the other models in almost all the regions.

Similar to the expression of the total Reynolds stress in (4.2), the turbulent heat flux takes the form

$$R_{u_jT} = \langle\bar{\rho}\rangle(\{\widetilde{u_j T}\} - \{\widetilde{u}_j\}\{\widetilde{T}\}) = R_{u_jT}^{LES} + \langle Q_j\rangle, \tag{4.4}$$

where

$$R_{u_jT}^{LES} = \langle\bar{\rho}\rangle(\{\widetilde{u}_j\widetilde{T}\} - \{\widetilde{u}_j\}\{\widetilde{T}\}) \tag{4.5}$$

is the resolved turbulent heat flux. Figure 6(b) presents the profiles of the normalized turbulent heat flux $R_{vT}/(\rho_w u_\tau T_w)$ from DNS, the DSM, the dk-equation model and the QKM. From figure 6(b), we can see that the QKM yields a precise prediction compared with the DNS, but the other models still have obvious deviations from the real value. And we also show the resolved Reynolds stress and the resolved turbulent heat flux in figure 7. From the figures, we see that the QKM can predict both the resolved part and the modelled part well. The dk-equation model can also obtain better results than the DSM does.

In figure 8(a–c), we present the profiles of the normalized resolved turbulence intensities $\widetilde{u}_i^{rms}/u_\tau = \langle(\widetilde{u}_i - \langle\widetilde{u}_i\rangle)^2\rangle^{1/2}/u_\tau$ obtained from the DNS and the compared SGS models. From figure 8, the three components of the resolved turbulence intensity predicted by the QKM are clearly much closer to the real values than those from the DSM and dk-equation model in all regions. Figure 8(d) shows the turbulent kinetic energy from DNS and the different models. From the figure, we see that the QKM can supply better results than the other SGS models including the total turbulent kinetic energy and ρk_{sgs}.

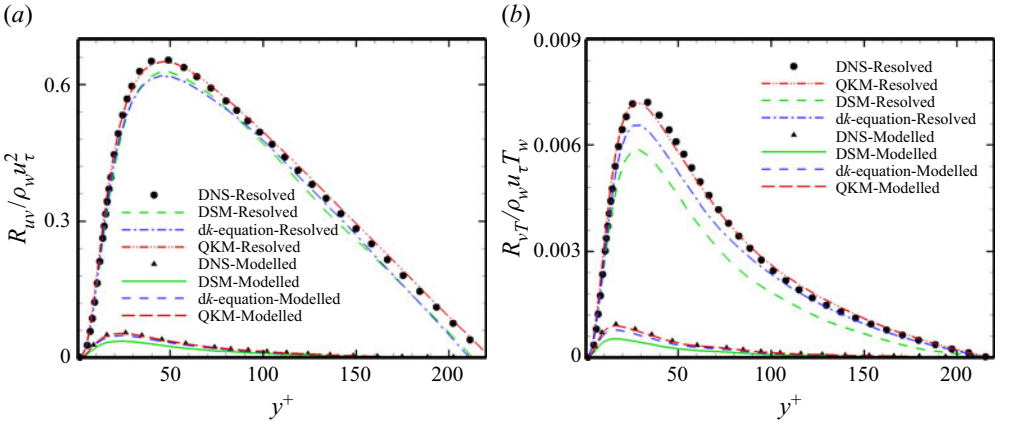

Figure 7. The profiles of the resolved Reynolds stress normalized by ρ_w and u_τ, and the resolved turbulent heat flux normalized by ρ_w, u_τ and T_w from DNS and different SGS models in the case of LES-grid2.

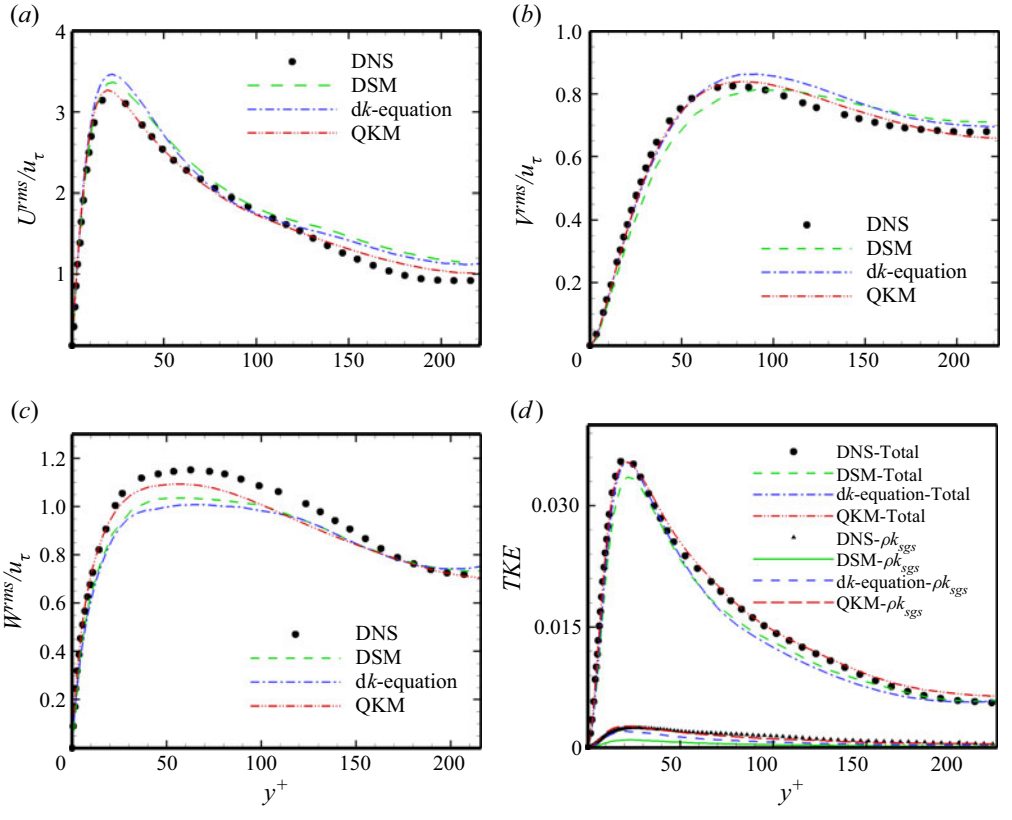

Figure 8. The profiles of the resolved turbulence intensities normalized by the friction velocity u_τ and the turbulent kinetic energy (TKE) from DNS and different SGS models in the case of LES-grid2: (*a*) streamwise turbulence intensity; (*b*) wall-normal turbulence intensity; (*c*) spanwise turbulence intensity; (*d*) the TKE $\frac{1}{2}R_{ii}$.

In compressible channel flows, density and temperature fluctuations also attract much attention. The profiles of the normalized resolved density fluctuation ρ^{rms}/ρ_{av} and temperature fluctuation T^{rms}/T_{av} predicted from DNS and the different SGS models are

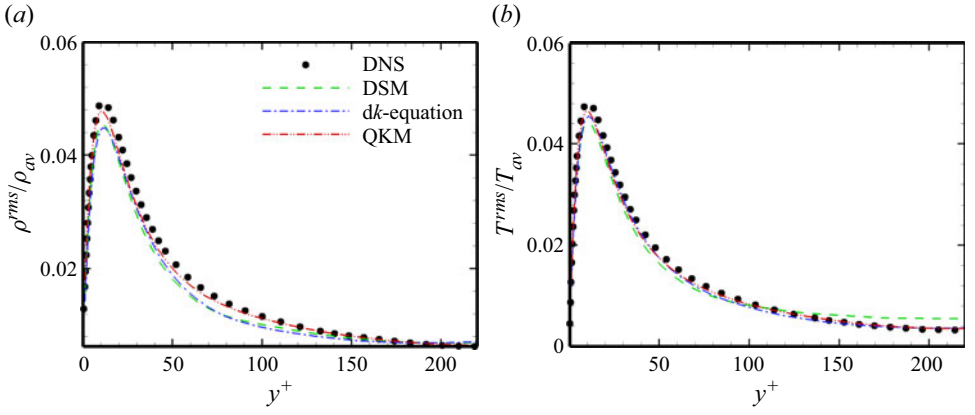

Figure 9. The profiles of the resolved root-mean-square (r.m.s.) density fluctuations normalized by averaged density ρ_{av} and the resolved r.m.s. temperature fluctuations normalized by averaged temperature T_{av} from DNS and different SGS models in the case of LES-grid2: (*a*) density fluctuations; (*b*) temperature fluctuations.

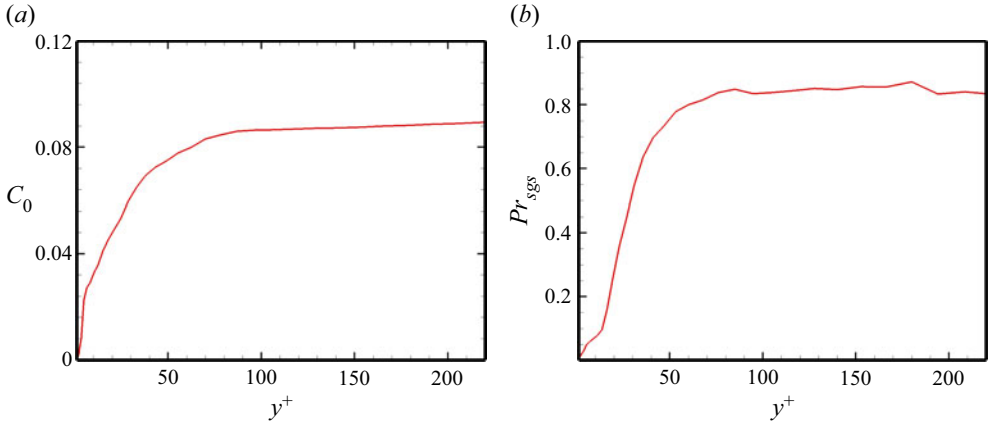

Figure 10. The profiles of C_0 and Pr_{sgs} obtained *a posteriori* for the compressible turbulent channel flow in the case of LES-grid2.

shown in figure 9, where ρ_{av} and T_{av} are the average density and temperature, respectively. As expected, the density and temperature fluctuations obtained from the QKM tightly match the profiles from DNS, which is a little better than the results of the other SGS models.

Next, we show the profiles of C_0 and Pr_{sgs} from the *a posteriori* test in figure 10. The values of C_0 and Pr_{sgs} have similar trends. Notably, the maximum value of C_0 is approximately 0.08 and the maximum value of Pr_{sgs} is approximately 0.8.

Then we compare the turbulent structure obtained from DNS and the different SGS models. Figure 11 shows the instantaneous isosurface of Q (second invariant of the strain-rate tensor, $Q = 0.25$) obtained from DNS, the QKM, the DSM and the dk-equation model. From figure 11, we can see that the QKM can predict more abundant structures, and in figure 11(*b*) there are many more small-scale vortexes than the results in figure 11(*c*,*d*), especially in the near-wall regions. Therefore, we infer that the QKM has a better ability to predict the turbulent structure.

To see the computational efficiency of the SGS models, we show the computing time per time step using 112 CPUs from different SGS models in table 5. Obviously, the QKM and dk-equation model take approximately the same time, slightly longer than the DSM.

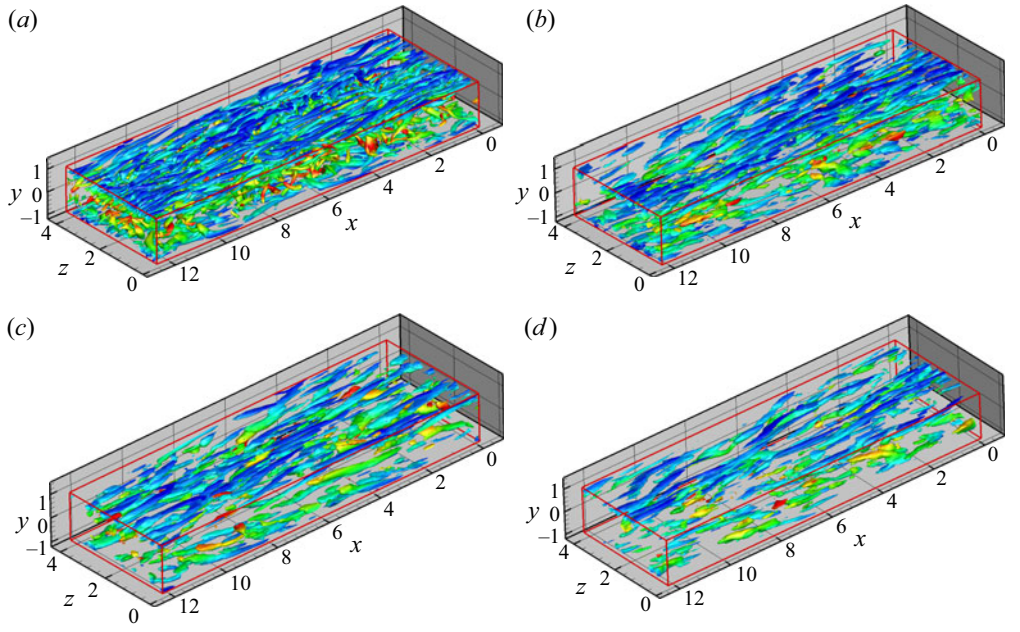

Figure 11. Instantaneous isosurface of Q (second invariant of the strain-rate tensor, $Q = 0.25$) obtained from (*a*) DNS, (*b*) the QKM, (*c*) the DSM, (*d*) the dk-equation model of compressible turbulent channel flow in the case of LES-grid2.

SGS model	DSM	dk-equation model	QKM
Time	4.13×10^{-2} s	7.38×10^{-2} s	7.22×10^{-2} s

Table 5. The computing time per time step using 112 CPUs for different SGS models.

	Grids	Δx^+	Δy^+_{min}	Δy^+_{max}	Δz^+
LES-grid	$86 \times 97 \times 86$	66.4	1.44	19.5	22.14

Table 6. The grid settings and grid resolutions of the simulations in the compressible turbulent channel flow ($Ma = 3.0$, $Re = 4880$).

To further test the new model in the case of a higher Mach number, we will discuss the results for the case of $Ma = 3.0$ and $Re = 4880$ (Coleman *et al.* 1995; De Stefano, Brown-Dymkoski & Vasilyev 2020). The size of the computational domain, the Prandtl number Pr, the boundary conditions, the ratio of specific heats and the setting of LES solver are the same with the case of $Ma = 1.5$ and $Re = 3000$. The grid resolutions and the main parameters of this case are listed in tables 6 and 7, respectively.

Figure 12 shows the profiles of the van Driest transformed mean velocity U_{vd} and mean temperature T^+_{av} obtained from different SGS models and DNS. Figure 13 shows the profiles of the total Reynolds stress and the turbulent heat flux normalized by ρ_w, u_τ and T_w from different SGS models and DNS. From the figures, we can see that the QKM can yield obviously better behaviour than the other models even in the case of higher

	Re_τ	Ma_τ	$-B_q$	u_c/U_m	ρ_c/ρ_w	T_c/T_w
DSM	444	0.101	0.125	1.21	0.399	2.69
dk-equation model	448	0.108	0.129	1.18	0.395	2.65
QKM	452	0.112	0.135	1.14	0.38	2.59

Table 7. The main parameters for the simulations in the compressible turbulent channel flow ($Ma = 3.0$, $Re = 4880$).

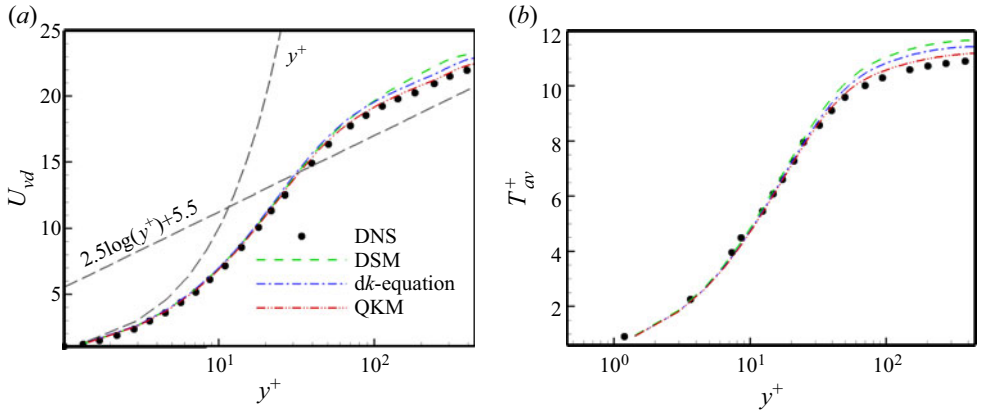

Figure 12. The profiles of the van Driest transformed mean velocity U_{vd} and mean temperature T^+_{av} obtained from different SGS models and DNS. The DNS results are from Coleman *et al.* (1995).

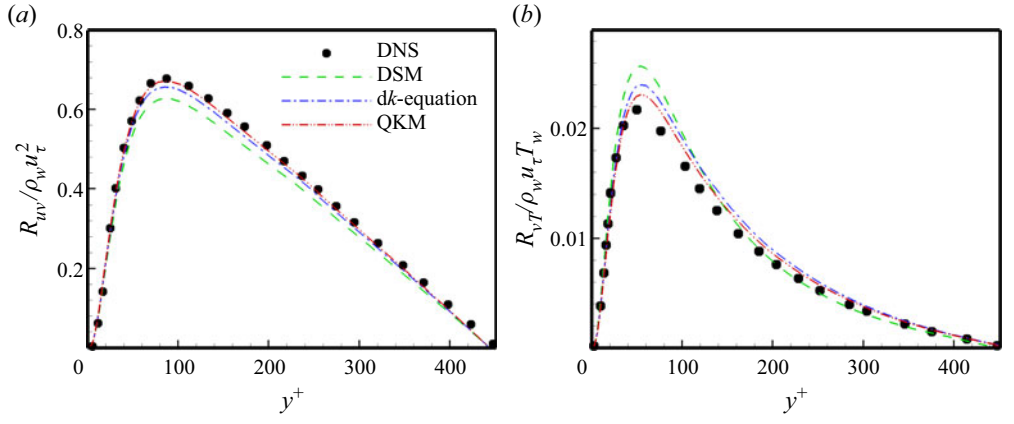

Figure 13. The profiles of the total Reynolds stress and the turbulent heat flux normalized by ρ_w, u_τ and T_w from different SGS models and DNS. The DNS results are from Coleman *et al.* (1995).

Mach number. At the same time, the dk-equation model can supply better predictions than the DSM.

4.2. *Application in compressible flat-plate boundary layer*

In this part, the newly proposed model is tested in the flow of the compressible flat-plate boundary layer. Unlike the channel flow, the compressible flat-plate boundary layer

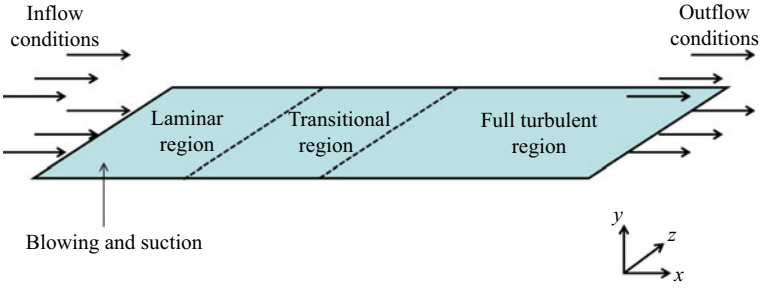

Figure 14. Sketch of the computational domain for the compressible flat-plate boundary layer.

	Grids	Δx^+	Δy^+_{min}	Δy^+_{max}	Δz^+
DNS	$10\,000 \times 90 \times 320$	6.0	0.58	185.5	5.47
LES-gridA	$1500 \times 90 \times 100$	40.1	0.58	185.5	17.5
LES-gridB	$1000 \times 90 \times 80$	60.2	0.58	185.5	21.9
LES-gridC	$1000 \times 60 \times 50$	60.2	1.00	264.8	35.1

Table 8. The grid settings and main parameters of the simulations in compressible flat-plate boundary layer ($Ma = 2.25$, $Re/in. = 635\,000$).

flow contains laminar, transitional and fully turbulent regions. Here, a typical spatially developing supersonic flat-plate boundary layer flow (Pirozzoli, Grasso & Gatski 2004) is chosen as a standard example. The simulation results from the DSM and dk-equation model are also selected for comparison. The computational domain is set to the same in-flow and out-flow boundary conditions as the standard example, the no-slip condition is used in the wall and the periodic condition is applied in the spanwise direction. Also, L (one inch) is the non-dimensionalizing length scale. Blow and suction disturbances are imposed near the wall at $4.5 < x/L < 5.0$ to trigger the transition, which is the same as the standard example except for the amplitude of the disturbances (0.02 is selected here). The size of the computational domain is $L_x \times L_y \times L_z = 6 \times 0.3 \times 0.175$. The sketch of the computational domain is shown in figure 14. The Mach number $Ma = 2.25$ and the free-stream unit Reynolds number $Re/in. = 635\,000$ are selected for this case. The grid resolution for DNS in this case is $10\,000 \times 90 \times 320$ with a spatial resolution of $\Delta x^+ = 6.02$, $\Delta z^+ = 5.47$, and minimum grid spacing in the wall-normal direction $\Delta y^+_w = 0.58$. Three different LES grid settings are selected for testing the models and the main parameters of the simulation in the compressible flat-plate boundary layer are listed in table 8.

First, we test the rationality of our assumption regarding C_0 in the compressible flat-plate boundary layer using the *a priori* test with DNS data at the scale of $3\Delta_z$ from the compressible flat-plate boundary layer in figure 15. From the figure, we can see that the values of C_0 obtained from the different expanded terms (τ_{ij}, Q_j, Π_p, ε_s and ε_d) still have a similar trend and value as the real results. The results from the *a priori* test confirm the validity of our assumption.

The distributions of the van Driest transformed mean velocity at $x/L = 8.8$ and the skin friction coefficient along the flat plate obtained from the different SGS models in three LES cases and DNS are displayed in figure 16. From figure 16(a1,a2) we can see that the results from the QKM precisely accord with the real values. The DSM and dk-equation

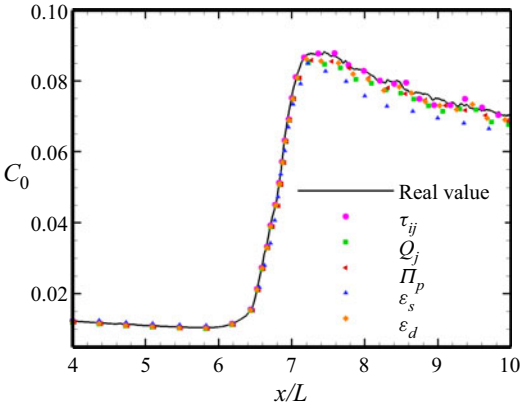

Figure 15. The profiles of C_0 along the streamwise direction at $y^+ = 15$ using the *a priori* test in the compressible flat-plate boundary layer.

model can also supply passable prediction results, including the mean velocity profile, the transition onset and the transition peak. For the case of grid-B, as seen from the simulation results in figure 16(*b*1,*b*2), the QKM can still supply accurate prediction results that are much better than those obtained from the DSM and d*k*-equation model. The results from the d*k*-equation model are better than those from the DSM. In the case of grid-C, the grid has the lowest resolution. Figure 16(*c*1,*c*2) shows that the QKM can still provide fairly good results, while the other two models cannot yield acceptable simulation results. Overall, from the results in figure 16, we could infer that the QKM can predict the mean quantities in compressible flat-plate boundary layer flow properly and that it also has good scale adaptivity.

Next, we will use the results from the case of grid-C to further explore the characteristics of the QKM. To further observe the prediction of the transition, we supply the profiles of the skin friction coefficient distribution vs Re_θ ($Re_\theta = \rho_\infty u_\infty \theta/\mu_\infty$ is a momentum thickness Reynolds number) from different SGS models and DNS in the case of grid-C in figure 17. The QKM maintains the best performance in predicting the transition onset and the transition peak, and the d*k*-equation model can also predict the transition process except the transition peak, but the prediction results of the DSM deteriorate distinctly.

In figure 18, we show the profiles of the normalized resolved turbulence intensities and the turbulent heat flux at $x/L = 8.8$ from the different SGS models and DNS in the case of grid-C. We can see that the streamwise turbulence intensities from the QKM, DSM and d*k*-equation model in figure 18(*a*) show no great difference, but the QKM shows better performance at $y^+ < 10$. The wall-normal and spanwise turbulence intensities in figures 18(*b*) and 18(*c*) have different behaviours and the results from the QKM are better than those from the other models. The d*k*-equation model behaves better than the DSM. From figure 18(*d*), we can see that the QKM could predict the turbulent heat flux well and that its results are better than those of the DSM and d*k*-equation model.

Figure 19 shows the *a posteriori* result of the KEF at $y^+ = 15$ from the different SGS models in the case of grid-C and the DNS value is displayed here for comparison (the KEF in figure 19(*a*) is from (3.2), and τ_{ij} is from (2.8)). From the figures, we can see that the QKM is much more similar to the real KEF than to the KEF from the other two models, including the distribution, the intensity, the sophisticated flow structure and even the energy backscatters. Similar to the prediction results of the KEF, the wall-normal SGS heat flux at $y^+ = 15$ (figure 20) predicted by the QKM shows much better behaviour than

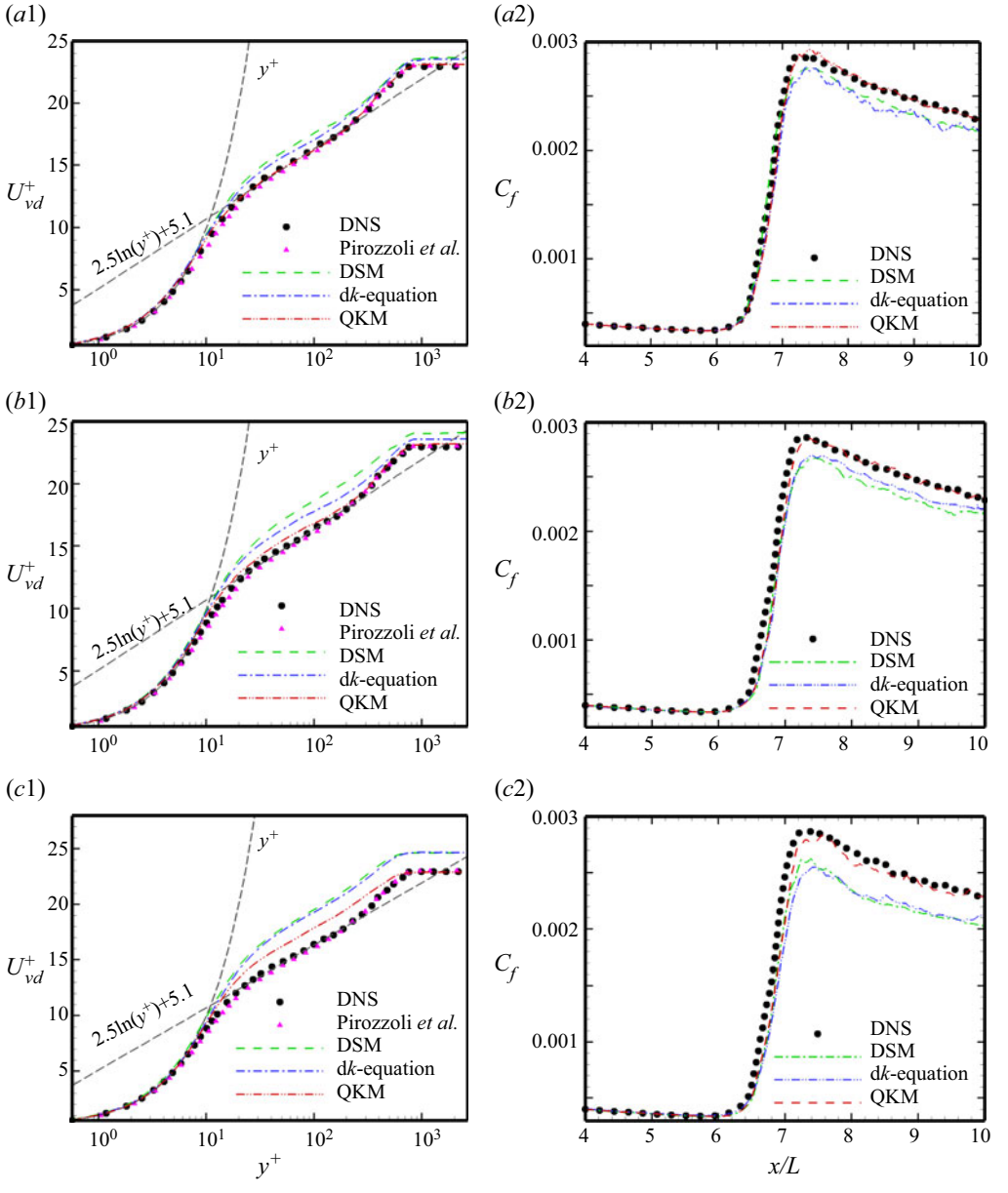

Figure 16. The profiles of the van Driest transformed mean velocity at $x/L = 8.8$ and the skin friction coefficient distribution along the flat plate from different SGS models and DNS: (*a*1) and (*a*2) show grid-A; (*b*1) and (*b*2) show grid-B; (*c*1) and (*c*2) show grid-C. The velocity profile from Pirozzoli *et al.* (2004) is also given here.

those of the other models compared with the real result (the SGS heat flux in figure 20(*a*) is from (2.9)).

4.3. *Application in spherical converging Richtmyer–Meshkov instability*

In this section, we will test the proposed model in the flow of spherical converging Richtmyer–Meshkov instability, which is a complicated time-developing case. As shown

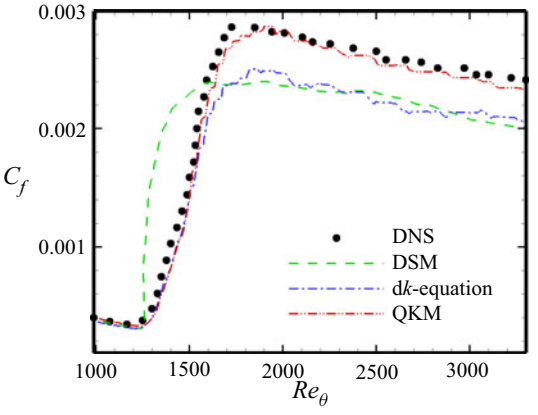

Figure 17. Profiles of skin friction coefficient distribution versus Re_θ from different SGS models and DNS in the case of grid-C.

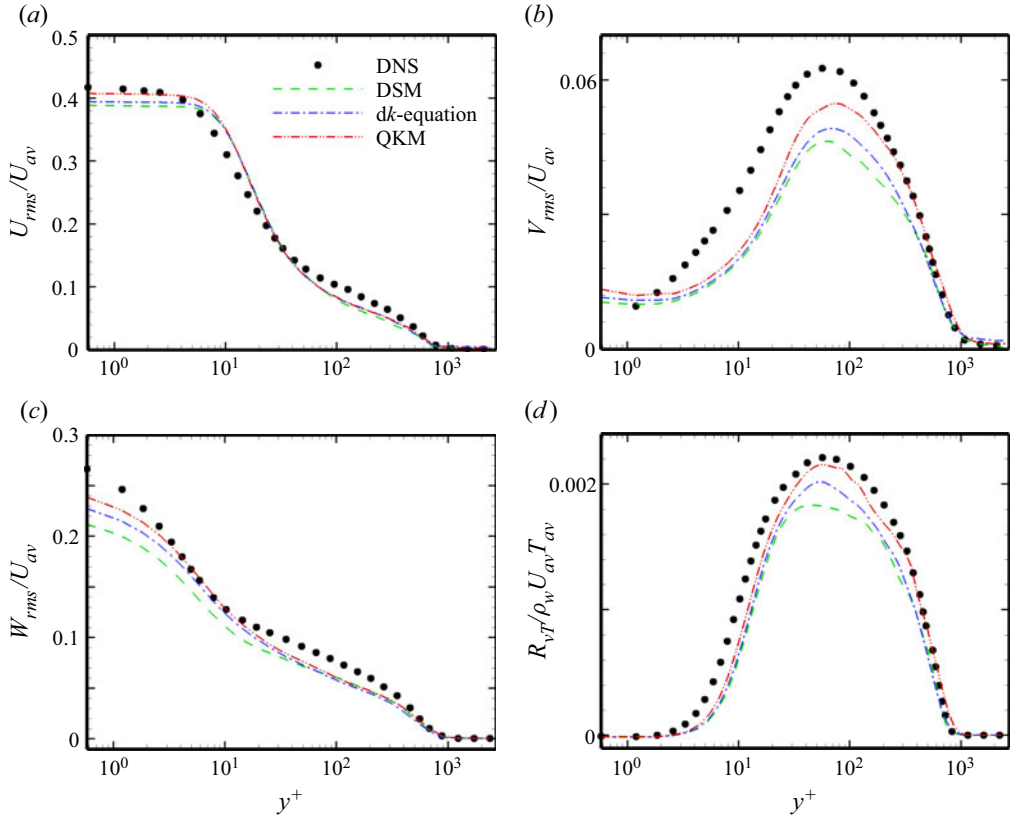

Figure 18. Profiles of the resolved turbulence intensities normalized by U_{av} and the turbulent heat flux normalized by $\rho_w U_{av} T_{av}$ at $x/L = 8.8$ from different SGS models and DNS in the case of grid-C: (*a*) streamwise turbulence intensity; (*b*) wall-normal turbulence intensity; (*c*) spanwise turbulence intensity; (*d*) the turbulent heat flux.

in figure 21, the shock wave converges from the heavy fluid into the light fluid in the flow. The heavy fluid is sulphur hexafluoride (SF_6) and the light fluid is nitrogen (N_2). In this case, the Mach number is approximately 1.5, and the Atwood number is

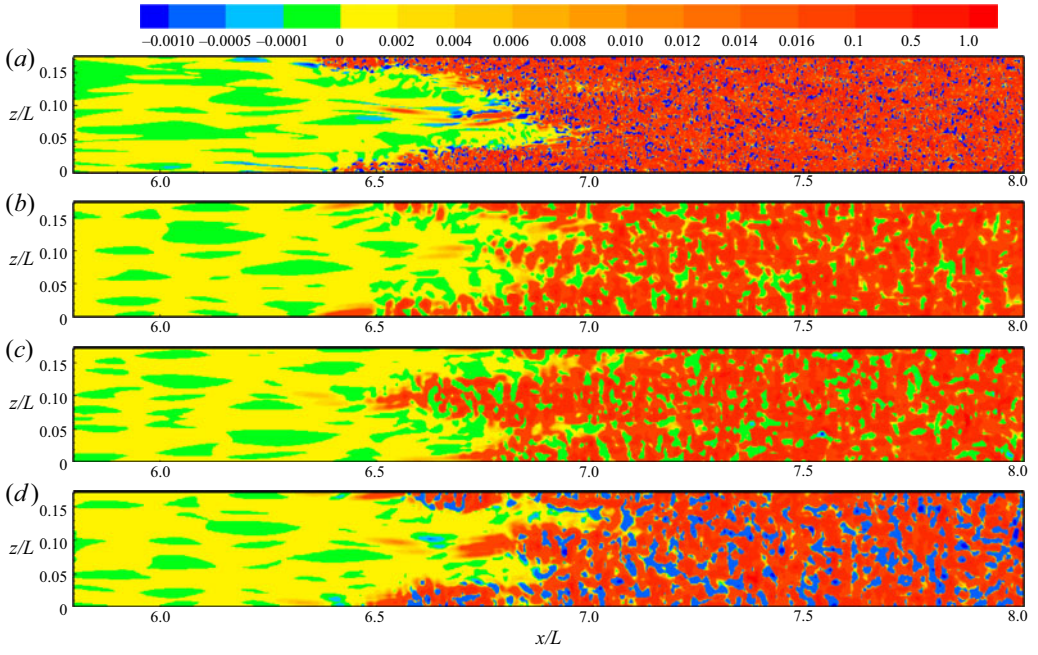

Figure 19. The *a posteriori* test of the KEF at $y^+ = 15$ from different SGS models in the case of grid-C and DNS results are displayed here for comparison: (*a*) DNS; (*b*) the DSM; (*c*) the d*k*-equation model; (*d*) the QKM.

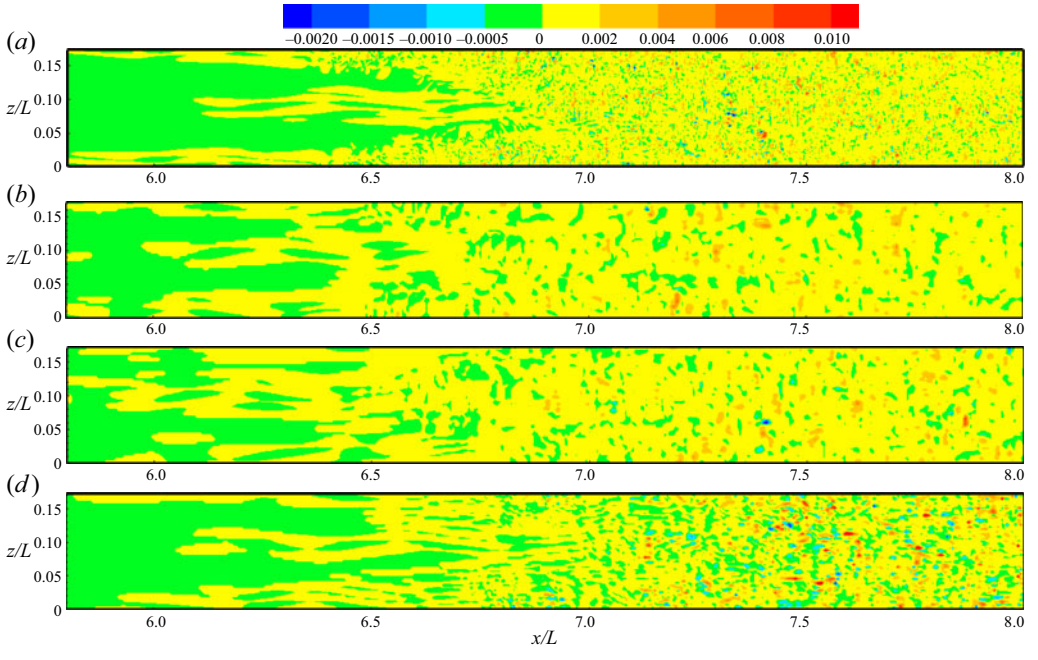

Figure 20. The *a posteriori* test of the wall-normal SGS heat flux at $y^+ = 15$ from different SGS models in the case of grid-C and DNS results are displayed here for comparison: (*a*) DNS; (*b*) the DSM; (*c*) the d*k*-equation model; (*d*) the QKM.

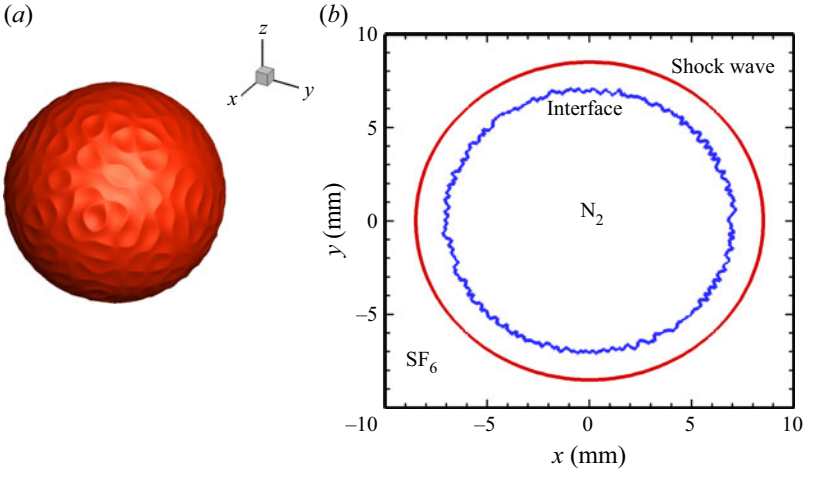

Figure 21. The isosurface of $Y_{SF_6} = 0.99$ for the spherical converging Richtmyer–Meshkov instability, and the shock wave and interface configuration diagram at the initial time: (*a*) isosurface of $Y_{SF_6} = 0.99$; (*b*) shock wave and interface configuration diagram.

	Pre-shock		Post-shock
	N_2	SF_6	SF_6
P/pa	101 325	101 325	233435.425
$\rho/(\mathrm{kg\,m^{-3}})$	1.145	5.971	12.748
$U_r/(\mathrm{m\,s^{-1}})$	0	0	108.456
γ	1.4	1.09	1.09

Table 9. The main parameters at the initial time (U_r is radial velocity).

Case	Grids
DNS	$2048 \times 2048 \times 2048$
LES	$384 \times 384 \times 384$

Table 10. The grid setting and the main parameters of the simulations in spherical converging Richtmyer–Meshkov instability (the Mach number is approximately 1.5, and the Atwood number is 0.678).

$A = (\rho_h - \rho_l)/(\rho_h + \rho_l) = 0.678$, where ρ_h and ρ_l are the densities of SF_6 and N_2 at the initial time, respectively. The main computational domain in the Cartesian coordinate system is $L_x = L_y = L_z = 20\,\mathrm{mm}$. The total uniform and structured Cartesian grid is applied in the main computational domain. To avoid the influence of boundary reflection, a sufficiently long sponge layer with 50 non-uniform coarse grids is added for each direction. To make sure that there is no singularity on the spherical surface, the spherical harmonic function is used to generate the initial perturbation (Lombardini, Pullin & Meiron 2014). The main parameters at the initial time and the grid setting of the simulations in the spherical converging Richtmyer–Meshkov instability are listed in tables 9 and 10, respectively.

The N–S equations are solved by the finite difference method. The mixing scheme combining the sixth-order monotonicity preserving optimized scheme (OMP6) (Li, Yan & He 2013) and eighth-order central difference scheme is adopted to discretize the convective terms. The eighth-order central difference scheme is employed for the viscous terms, and the third-order Runge–Kutta approach is taken for the time integration (Hill, Pantano & Pullin 2006; Bin *et al.* 2021).

The filtered N–S equations are the same as (2.1)–(2.3). For solving the spherical converging Richtmyer–Meshkov instability, the filtered equation for the mass fraction of species (Hill *et al.* 2006; Lombardini *et al.* 2011) is introduced as

$$\frac{\partial \bar{\rho}\tilde{Y}_k}{\partial t} + \frac{\partial \bar{\rho}\tilde{Y}_k\tilde{u}_j}{\partial x_j} = \frac{\partial}{\partial x_j}\left(\bar{\rho}D_{km}\frac{\partial \widetilde{Y}_k}{\partial x_j} - Y_{j,k}^{sgs}\right), \tag{4.6}$$

where Y_k is the mass fraction of species k, D_{km} denotes the mixture diffusion coefficients of species k which are obtained from the Schmidt number $Sc_k = \mu(\widetilde{T})/\bar{\rho}D_{km} = 1$, and the SGS species flux $Y_{j,k}^{sgs} = \bar{\rho}(\widetilde{Y_k u_j} - \widetilde{Y}_k\widetilde{u}_j)$ is an unclosed term, which can be modelled as

$$Y_{j,k}^{sgs} = -\frac{\mu_{sgs}}{Sc_{sgs,k}}\frac{\partial \widetilde{Y}_k}{\partial x_j}, \tag{4.7}$$

where μ_{sgs} is the SGS eddy viscosity and $Sc_{sgs,k}$ is the SGS Schmidt number.

Similar to the solution process of Pr_{sgs}, $Sc_{sgs,k}$ for the newly proposed model can be obtained as

$$Sc_{sgs,k} = -\frac{\partial\left(\nu_{sgs}\dfrac{\partial \widetilde{Y}_k}{\partial x_j}\right)/\partial x_j}{\partial\left(C_0\Delta_m^2\dfrac{\partial \widetilde{u}_j}{\partial x_m}\dfrac{\partial \widetilde{Y}_k}{\partial x_m}\right)/\partial x_j}. \tag{4.8}$$

The constant-coefficient SM is also selected for comparison here. The model coefficient of the SM is chosen as 0.1. Pr_{sgs} and $Sc_{sgs,k}$ for the constant-coefficient model are set as 0.9 and 0.35, respectively.

Figure 22 shows the evolution of the inner and outer radii of the mixing layer with the time obtained from different models and DNS. The inner radius r_1 is the position where the mass fraction of the heavy fluid is 0.01 and the outer radius r_2 is the position where the mass fraction of the light fluid is 0.01. For the inner radius, the QKM can obtain proper results at almost time, DSM and dk-equation model show deviation from the DNS result during $0.075\,\text{ms} < t < 0.12\,\text{ms}$, and the SM shows worse prediction during $0.04 < t < 0.12\,\text{ms}$. For the outer radius, the QKM can accurately predict the evolution profile and still perform better than the DSM, dk-equation model and SM. The DSM and dk-equation model have better predictions than the SM in most of area.

Then, the evolution profiles of the heights of the bubble (where light fluid penetrates heavy fluid) and spike (where heavy fluid penetrates light fluid) obtained from DNS and the different SGS models are compared in figure 23. According to the inner and outer radii of the mixing layer, the heights of the bubble and spike are given as

$$h_b = r_2 - r_{0.5}, \tag{4.9}$$

$$h_s = r_1 - r_{0.5}, \tag{4.10}$$

where $r_{0.5}$ is the position where the mass fractions of light and heavy fluids are both 0.5. The SM cannot predict the heights of the bubble and spike, and it grossly underestimates

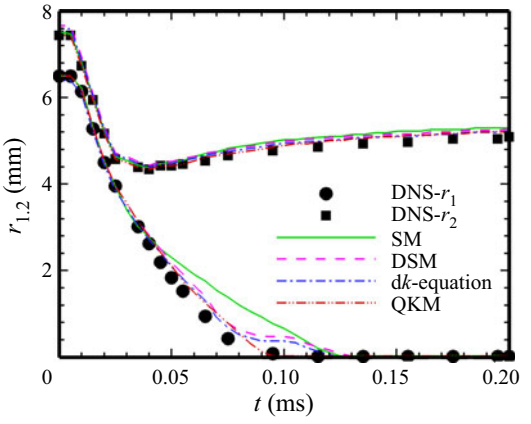

Figure 22. The evolution of the inner and outer radii of the mixing layer with the time obtained from different SGS models and DNS.

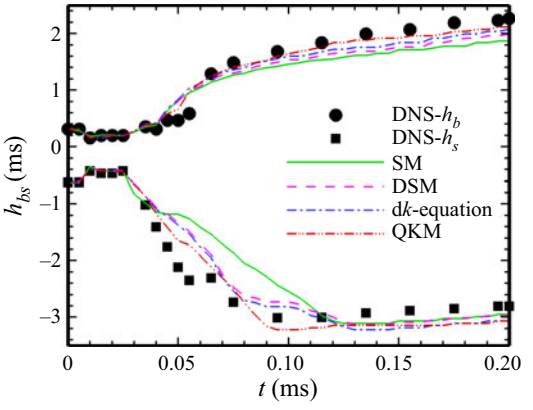

Figure 23. The evolution of the heights of the bubble and spike with the time obtained from different SGS models and DNS.

their values, especially during $0.04 < t < 0.12$ ms. In contrary, the QKM can still yield passable results during the whole process.

From figures 22 and 23, we could infer that the turbulent mixing begins at $t = 0.04$ ms and ends at 0.12 ms, which accords with the conclusion that the SM cannot successfully predict the transition process (Piomelli & Zang 1991; Meneveau & Katz 2000; Sayadi & Moin 2012; Zhou *et al.* 2019). At the same time, we can see that the results from the DSM and dk-equation model show deviation from DNS results during $0.075\,\text{ms} < t < 0.12$ ms, obviously. Perhaps, it is caused by strong anisotropy and inhomogeneity of the flow during $0.075\,\text{ms} < t < 0.12$ ms, which cannot meet the requirement of scale invariance for the traditional dynamic procedure. And it also proves that the QKM can predict the turbulent mixing process well.

Then, we select the results of the density distribution in the x–y plane and the isosurfaces of the mass fraction of SF_6 from DNS, QKM and the SM at two moments ($t = 0.08$ and $t = 0.12$ ms), shown in figures 24 and 25. From figures 24 and 25, we can see that the QKM is much more similar to DNS than the SM, including the spatial distributions of the different species and the locations of the converging surfaces. We have seen again that the QKM can provide sufficiently abundant turbulent structures.

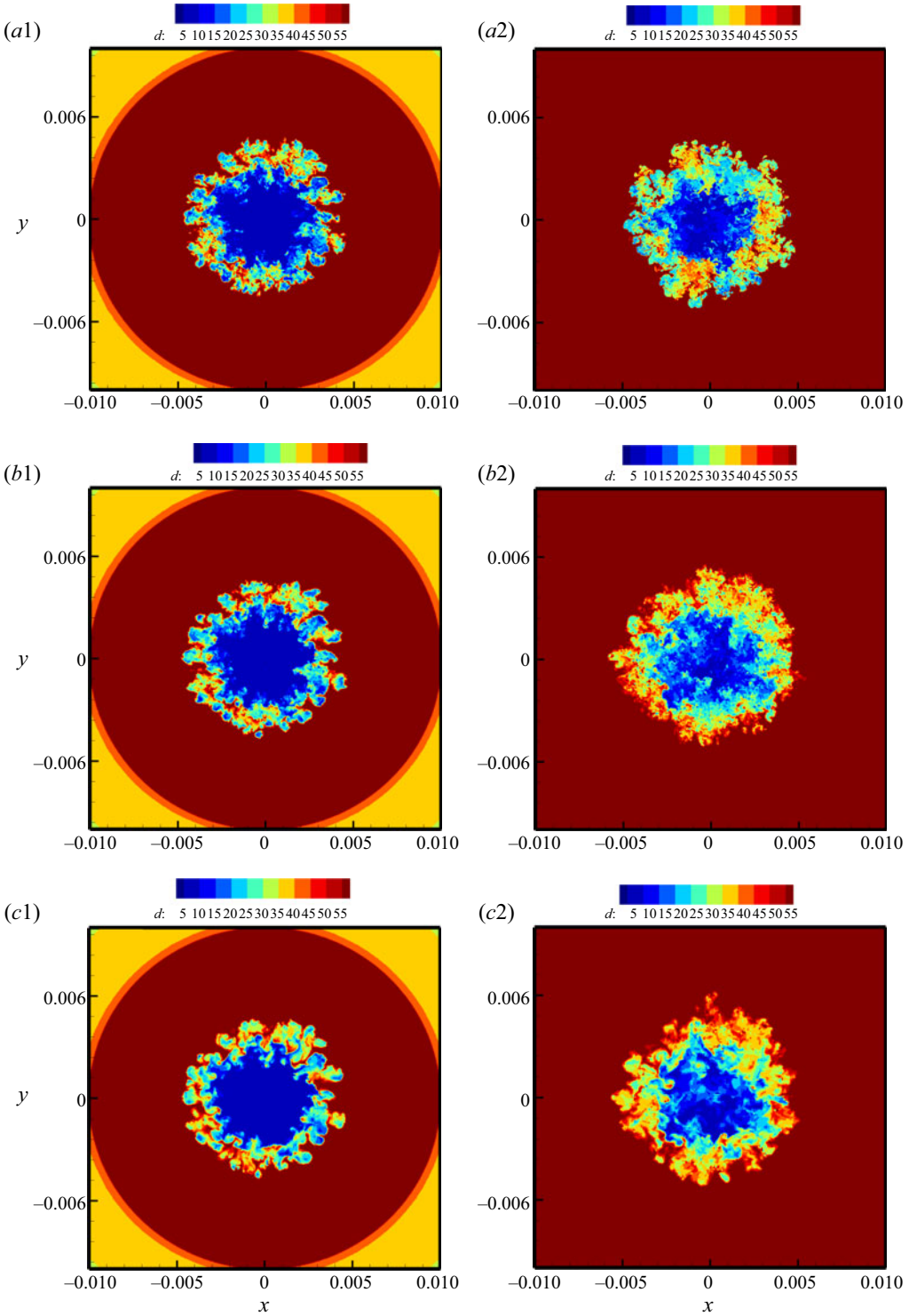

Figure 24. The density distribution in the x–y plane: (a1,b1,c1) are at $t = 0.08$ ms; (a2,b2,c2) are at $t = 0.2$ ms; (a1,a2) are from DNS; (b1,b2) are from the QKM; (c1,c2) are from the SM.

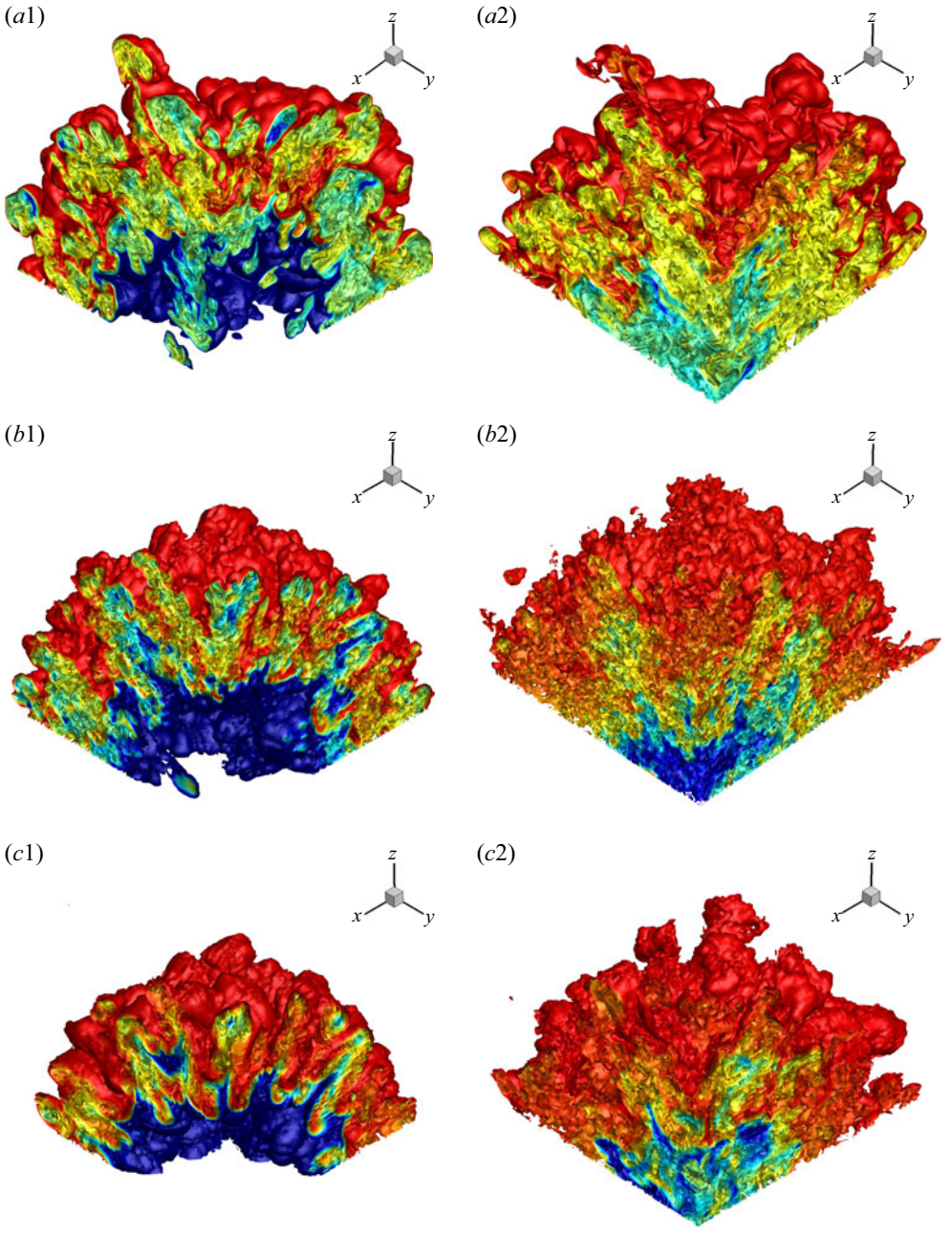

Figure 25. The isosurfaces of the mass fraction of SF_6: (a1,b1,c1) are at $t = 0.08$ ms; (a2,b2,c2) are at $t = 0.2$ ms; (a1,a2) are from DNS; (b1,b2) are from the QKM; (c1,c2) are from the SM (Only one eighth of the main computational domain is shown).

5. Conclusions

In this paper, we propose a QKM for LES of compressible flows. First, the SGS kinetic energy equation is introduced to constrain the first term of the expanded SGS stress to obtain a more accurate resolved SGS stress, and thus the coefficient of the first term

can also be determined. Then, using the accurate resolved SGS stress, we obtain the precise SGS KEF, which can be adopted to constrain the Smagorinsky model. With the dual constraints of the SGS kinetic energy and KEF, a new SGS eddy-viscosity model is confirmed. Similar to the expanded SGS stress, other unclosed quantities can be also expanded by the same infinite series expansion, and their first terms are also reserved as their approximate models. To obtain more exact models, the coefficients of these first terms take the same values as those of the expanded SGS stress, which is proved by the *a priori* test. Following the similar constraint criterion on the SGS stress model, the SGS heat flux model and SGS species flux model can be also obtained precisely. All the coefficients of these proposed models are resolved dynamically with no test filtering, and thus it can be regarded as a quasi-dynamic process. In this study, each of the unclosed quantities is modelled individually, and the newly proposed models combine the merits of strong numerical robustness and high correlation with the real SGS stress together, which has been proved by *a priori* and *a posteriori* tests.

The QKM is first employed to LES of the compressible turbulent channel flow. Compared with DNS, the DSM and the dynamic k-equation model, the QKM shows the good predictive power in the representative physical quantities, including the mean velocity, the mean temperature, the turbulence intensities, the turbulent heat and the Reynolds stress, etc. And the suggested model can also predict more abundant coherent structures in the channel flow. For the case of a supersonic spatially developing flat-plate flow, the QKM can well predict the transition process including the transition onset and peak, the mean velocity profile in turbulent region, the KEF, etc. At the same time, the new model also shows better scale adaptivity, as seen from the simulation results. When applied to the simulation in the spherical converging Richtmyer–Meshkov instability, which is a time-developing complex flow, the QKM can also show credible predictive power for the inner and outer radii of the mixing layer, the width of the mixing layer, the heights of the bubble and spike, etc.

In summary, the newly proposed QKM combines the merits of both the eddy-viscosity model and the gradient model, and the local coefficients of the QKM are determined dynamically. At same time, the QKM can predict the SGS KEF of the flow more precisely, which means that the QKM can descript the turbulent cascade accurately, and it could be regarded as the key factor for improving the prediction of turbulent flows. We anticipate that this model could be easily applied to the simulation of engineering flows with complex-geometry boundaries.

Funding. This work was supported by the National Key Research and Development Program of China (grant nos 2020YFA0711800 and 2019YFA0405302) and NSFC Projects (nos 12072349, 91852203), National Numerical Windtunnel Project, Science Challenge Project (grant no. TZ2016001) and Strategic Priority Research Program of Chinese Academy of Sciences (grant no. XDC01000000). The authors thank the National Supercomputer Center in Tianjin (NSCC-TJ) and the National Supercomputer Center in GuangZhou (NSCC-GZ) for providing computer time.

Declaration of interests. The authors report no conflict of interest.

Author ORCIDs.
Changping Yu https://orcid.org/0000-0002-2126-1344.

References

Bardina, J., Ferziger, J.H. & Reynolds, W.C. 1984 Improved turbulence models based on large-eddy simulation of homogeneous incompressible turbulent flows. *Rep. No.* TF-19, Department of Mechanical Engineering, Stanford.

BEDFORD, K.W. & YEO, W.K. 1993 Conjunctive filtering procedures in surface water flow and transport. In *Large Eddy Simulation of Complex Engineering and Geophysical Flows* (ed. B. Galperin & S.A. Orszag), pp. 513–539. Cambridge University Press.

BIN, Y., XIAO, M., SHI, Y., ZHANG, Y. & CHEN, S. 2021 A new idea to predict reshocked Richtmyer-Meshkov mixing: constrained large-eddy simulation. *J. Fluid Mech.* **918**, R1.

BORUE, V. & ORSZAG, S. 1998 Local energy flux and subgrid-scale statistics in three-dimensional turbulence. *J. Fluid Mech.* **366**, 1–31.

CHAI, X. & MAHESH, K. 2012 Dynamic *k*-equation model for large-eddy simulation of compressible flows. *J. Fluid Mech.* **699**, 385–413.

CLARK, R.A., FERZIGER, J.H. & REYNOLDS, W.C. 1979 Evaluation of subgrid-scale models using an accurately simulated turbulent flow. *J. Fluid Mech.* **91**, 1–16.

COLEMAN, G.N., KIM, J. & MOSER, R.D. 1995 A numerical study of turbulent supersonic isothermal-wall channel flow. *J. Fluid Mech.* **305**, 159–183.

DE STEFANO, G., BROWN-DYMKOSKI, E. & VASILYEV, O.V. 2020 Wavelet-based adaptive large-eddy simulation of supersonic channel flow. *J. Fluid Mech.* **901**, A13.

EYINK, G.L. 2006 Multi-scale gradient expansion of the turbulent stress tensor. *J. Fluid Mech.* **549**, 159–190.

GARNIER, E., ADAMS, N. & SAGAUT, P. 2013 *Large Eddy Simulation for Compressible Flows*. Springer.

GENIN, F. & MENON, S. 2010 Dynamics of sonic jet injection into supersonic crossflow. *J. Turbul.* **11** (4), 30.

GERMANO, M. 1992 Turbulence: the filtering approach. *J. Fluid Mech.* **238**, 325–336.

GERMANO, M., PIOMELLI, U., MOIN, P. & CABOT, W.H. 1991 A dynamic subgrid-scale eddy viscosity model. *Phys. Fluids* A **3** (7), 1760–1765.

GHOSAL, S., LUND, T.S., MOIN, P. & AKSELVOLL, K. 1995 A dynamic localization model for large-eddy simulation of turbulent flows. *J. Fluid Mech.* **286**, 229–255.

HILL, D.J., PANTANO, C. & PULLIN, D.I. 2006 Large-eddy simulation and multiscale modelling of a Richtmyer-Meshkov instability with reshock. *J. Fluid Mech.* **557**, 29–61.

HORIUTI, K. 1985 Large-eddy simulation of turbulent channel flow by one-equation modeling. *J. Phys. Soc.* **54** (8), 2855–2865.

HORIUTI, K. 1997 A new dynamic two-parameter mixed model for large-eddy simulation. *Phys. Fluids* **9** (11), 3443–3464.

HORIUTI, K. & TAMAKI, T. 2013 Nonequilibrium energy spectrum in the subgrid-scale one-equation model in large-eddy simulation. *Phys. Fluids* **25**, 125104.

KIM, W.W. & MENON, S. 1999 An unsteady incompressible Navier–Stokes solver for large eddy simulation of turbulent flows. *Intl J. Numer. Meth. Fluids* **31** (6), 983–1017.

LEONI, P.C.D., ZAKI, T.A., KARNIADAKIS, G. & MENEVEAU, C. 2021 Two-point stress-strain-rate correlation structure and non-local eddy viscosity in turbulent flows. *J. Fluid Mech.* **914**, A6.

LI, X., YAN, L. & HE, Z. 2013 Optimized sixth-order monotonicity-preserving scheme by nonlinear spectral analysis. *Intl J. Numer. Meth. Fluids* **73**, 560–577.

LILLY, D.K. 1967 On the application of the eddy viscosity concept in the inertial sub-range of turbulence. *NCAR Manuscript*, p. 123.

LILLY, D.K. 1992 A proposed modification of the Germano subgrid-scale closure method. *Phys. Fluids* A **4** (3), 633–635.

LIU, S., MENEVEAU, C. & KATZ, J. 1994 On the properties of similarity subgrid-scale models as deduced from measurements in a turbulent jet. *J. Fluid Mech.* **275**, 83–119.

LOMBARDINI, M., HILL, D.J., PULLIN, D.I. & MEIRON, D.I. 2011 Atwood ratio dependence of Richtmyer-Meshkov flows under reshock conditions using large-eddy simulations. *J. Fluid Mech.* **670**, 439–480.

LOMBARDINI, M., PULLIN, D.I. & MEIRON, D.I. 2014 Turbulent mixing driven by spherical implosions. Part 1. Flow description and mixing-layer growth. *J. Fluid Mech.* **748**, 85–112.

MARTÍN, M.P., PIOMELLI, U. & CANDLER, G.V. 2000 Subgrid-scale models for compressible large-eddy simulation. *Theor. Comput. Fluid Dyn.* **13** (5), 361–376.

MENEVEAU, C. 2012 Germano identity-based subgrid-scale modeling: a brief survey of variations on a fertile theme. *Phys. Fluids* **24** (12), 121301.

MENEVEAU, C. & KATZ, J. 2000 Scale-invariance and turbulence models for large-eddy simulation. *Annu. Rev. Fluid Mech.* **32** (1), 1–32.

MENEVEAU, C., LUND, T.S. & CABOT, W.H. 1996 A Lagrangian dynamic subgrid-scale model of turbulence. *J. Fluid Mech.* **319**, 353–385.

METAIS, O. & LESIEUR, M. 1992 Spectral large-eddy simulation of isotropic and stably stratified turbulence. *Annu. Rev. Fluid Mech.* **239**, 157–94.

MOENG, C.H. 1984 A large-eddy simulation model for the study of planetary boundary-layer turbulence. *J. Atmos. Sci.* **41** (13), 2052–2062.

MOIN, P., SQUIRE, K., CABOT, W. & LEE, S. 1991 A dynamic subgrid-scale model for compressible turbulence and scalar transport. *Phys. Fluids* A **3**, 2746–2757.

MORINISHI, Y., TAMANO, S. & NAKABAYASHI, K. 2004 Direct numerical simulation of compressible turbulent channel flow between adiabatic and isothermal walls. *J. Fluid Mech.* **502**, 273–308.

MOSER, R.D., HAERING, S.W. & YALLA, G.R. 2021 Statistical properties of subgrid-scale turbulence models. *Annu. Rev. Fluid Mech.* **53** (1), 255–286.

NICOUD, F. & DUCROS, F. 1999 Subgrid-scale stress modelling based on the square of the velocity gradient tensor. *Flow Turbul. Combust.* **63**, 183–200.

NICOUD, F., TODA, H.B., CABRIT, O., BOSE, S. & LEE, J. 2011 Using singular values to build a subgrid-scale model for large-eddy simulations. *Phys. Fluids* **23**, 085106.

PATEL, N., STONE, C. & MENON, S. 2003 Large-eddy simulation of turbulent flow over an axisymmetric hill. *AIAA Paper* 2003-976.

PIOMELLI, U. & ZANG, T.A. 1991 Large-eddy simulation of transitional channel flow. *Comput. Phys. Commun.* **65**, 224–230.

PIROZZOLI, S., GRASSO, F. & GATSKI, T.B. 2004 Direct numerical simulation and analysis of a spatially evolving supersonic turbulent boundary layer at $m = 2.25$. *Phys. Fluids* **16** (3), 530–545.

POMRANING, E. & RUTLAND, C.J. 2002 Dynamic one-equation nonviscosity large-eddy simulation model. *AIAA J.* **40** (4), 689–701.

PORTE-AGEL, F., MENEVEAU, C. & PARLANGE, M.B. 2000 A scale-dependent dynamic model for large-eddy simulation: application to a neutral atmospheric boundary layer. *J. Fluid Mech.* **415**, 261–284.

RONCHI, C., YPMA, M. & CANUTO, V.M. 1992 On the application of the Germano identity to subgrid-scale modeling. *Phys. Fluids* A **4** (12), 2927–2929.

ROZEMA, W., BAE, H.J., MOIN, P. & VERSTAPPEN, R. 2015 Minimum-dissipation models for large-eddy simulation. *Phys. Fluids* **27**, 085107.

SAYADI, T. & MOIN, P. 2012 Large eddy simulation of controlled transition to turbulence. *Phys. Fluids* **24**, 114103.

SCHUMANN, U. 1975 Subgrid scale model for finite difference simulations of turbulent flows in plane channels and annuli. *J. Comput. Phys.* **18** (4), 376–404.

SMAGORINSKY, J. 1963 General circulation experiments with the primitive equations: I. The basic experiment. *Mon. Weath. Rev.* **91**, 99–164.

STEVENS, B., MOENG, C.H. & SULLIVAN, P.P. 1999 Large-eddy simulation of radiatively driven convection: sensitivities to the representation of small scales. *J. Atmos. Sci.* **56**, 3963–3984.

TEJADA-MARTÍNEZ, A.E. & JANSEN, K.E. 2004 A dynamic smagorinsky model with dynamic determination of the filter width ratio. *Phys. Fluids* **16** (7), 2514–2528.

VREMAN, A.W. 2004 An eddy-viscosity subgrid-scale model for turbulent shear flow: algebraic theory and applications. *Phys. Fluids* **16**, 3670–3681.

VREMAN, B., GEURTS, B. & KUERTEN, H. 1994 On the formulation of the dynamic mixed subgrid-scale model. *Phys. Fluids* **6**, 4057–4059.

VREMAN, B., GEURTS, B. & KUERTEN, H. 1996 Large-eddy simulation of the temporal mixing layer using the Clark model. *Theor. Comput. Fluid Dyn.* **8** (4), 309–324.

WANG, B.-C., YEE, E., BERGSTROM, D.J. & IIDA, O. 2008 New dynamic subgrid-scale heat flux models for large-eddy simulation of thermal convection based on the general gradient diffusion hypothesis. *J. Fluid Mech.* **604**, 125–163.

WONG, V.C. 1992 A proposed statistical-dynamic closure method for the linear or nonlinear subgrid-scale stress. *Phys. Fluids* A **4** (5), 1080–1082.

YOSHIZAWA, A. 1986 Statistical theory for compressible turbulent shear flows, with the application to subgrid modeling. *Phys. Fluids* **29**, 2255–2271.

YOSHIZAWA, A. 1991 A statistically-derived subgrid model for the large-eddy simulation of turbulence. *Phys. Fluids* A **3** (8), 2007–2009.

YOSHIZAWA, H.K. 1985 A statistically-derived subgrid-scale kinetic energy model for the large-eddy simulation of turbulent flows. *J. Phys. Soc. Japan* **54** (8), 2834–2839.

YU, C., HONG, R., XIAO, Z. & CHEN, S. 2013 Subgrid-scale eddy viscosity model for helical turbulence. *Phys. Fluids* **25**, 095101.

YU, C., XIAO, Z. & LI, X. 2017 Scale-adaptive subgrid-scale modelling for large-eddy simulation of turbulent flows. *Phys. Fluids* **29** (3), 035101.

YU, C., ZUOLI, X. & XINLIANG, L. 2016 Dynamic optimization methodology based on subgrid-scale dissipation for large eddy simulation. *Phys. Fluids* **28**, 015113.

YUAN, Z., XIE, C. & WANG, J. 2020 Deconvolutional artificial neural network models for large eddy simulation of turbulence. *Phys. Fluids* **32** (11), 115106.

ZANG, Y., STREET, R.L. & KOSEFF, J.R. 1993 A dynamic mixed subgrid-scale model and its application to turbulent recirculating flows. *Phys. Fluids* A **5**, 3186–3196.

ZHOU, H., LI, X., QI, H. & YU, C. 2019 Subgrid-scale model for large-eddy simulation of transition and turbulence in compressible flows. *Phys. Fluids* **31**, 125118.